Research paper

A numerical study of drift angle effect on hydrodynamic performance of a fully appended container ship in head waves

Yifu Zhang [a,b,*], Héctor Rubén Díaz-Ojeda [c,**], Björn Windén [d], Dominic Hudson [a], Stephen Turnock [a]

[a] *Maritime Engineering, University of Southampton, Boldrewood Campus, Southampton, SO16 7QF, Hampshire, UK*
[b] *High Performance Computing (HPC) Team, University of Southampton, Highfield Campus, Southampton, SO17 1BJ, Hampshire, UK*
[c] *Universidad de Las Palmas de Gran Canaria (ULPGC), Las Palmas de Gran Canaria, 35001, Spain*
[d] *The Department of Ocean Engineering, Texas A&M University, 727 Ross Street, College Station, 77843, TX, USA*

ARTICLE INFO

ABSTRACT

To accurately predict the ship's manoeuvring and powering performance in actual seaways, it is crucial to gain an enhanced comprehension of the hydrodynamic behaviour of vessels navigating through waves. A critical component is the accurate determination of forces exerted on the hull and its appendages when the ship is operating at an angle of drift in waves. This is also significant for wind-assisted ships, which often operate with non-zero drift and rudder angles. Therefore, a deeper understanding of how drift and rudder angles affect hull–propeller–rudder interaction is required for investigating energy efficiency in waves. In this paper, a thorough numerical study is conducted to investigate the hydrodynamic interaction among the hull, propeller and rudder of the benchmark KRISO Container Ship (KCS) in regular head waves. The KCS is simulated at drift angles of −10°, 0° and +10°, combined with a series of rudder angles (−20° to +20°), representing quasi-static phases of actual ship manoeuvring in waves. Blade Element Momentum theory (BEMt) is adopted for modelling propeller action in all cases. Good agreement is found between experimental and numerical predictions regarding hull forces. This study contributes to better ship design due to ship manoeuvring and operations of wind-assisted vessels.

1. Introduction

Accurate prediction of ship powering and manoeuvring performance in waves is of high importance for the design of new vessels because it is related to ship safety, reliability, and overall efficiency. Meanwhile, the implementation of the EEDI has heightened concerns about the manoeuvrability of ships in wave conditions. In response, the IMO established a guideline titled "Minimum propulsion power to maintain manoeuvrability of ships in adverse conditions" (MEPC, 2017). According to the Specialist Committee on Manoeuvring in Waves (ITTC, 2021), accurately assessing how a vessel manoeuvres in waves remains a challenging task due to the intricate overlap between manoeuvrability and other critical factors including ship resistance, propulsion, and seakeeping. The interaction effects among these elements further complicate the estimation of manoeuvring in waves. Typically, challenges related to ship manoeuvring in waves can be addressed through experimental and numerical methods.

Experimental approaches for evaluating ship manoeuvrability include free-running model testing and captive model tests. For free-running test, Sanada et al. (2013) conducted turning tests on the ONR Tumblehome in calm and wave conditions at the IIHR wave basin of the University of Iowa and presented 6-DOF motion histories. Furthermore, Sanada et al. (2019) analysed the impact of ship speed and wave-length on manoeuvrability through repeat turning and zig-zag tests with the measured accuracy. Sprenger et al. (2017) and Shigunov et al. (2018) conducted turning and zig-zag manoeuvre tests for DTC container ship and KVLCC2 tanker models in regular waves, adjusting wave directions and wavelengths. Hasnan et al. (2020) presented the turning test results for ships with a rudder angle of ±30 degrees in short-crested irregular waves, utilizing models of a tanker (KVLCC2) and a container ship (KCS). Conducting captive model tests in waves is also crucial for assessing the forces and moments exert on manoeuvring ships. Yasukawa and Faizul (2006) and Yasukawa et al. (2010) studied the motions of an obliquely moving ship in regular waves, focusing on the S-175 container ship in head and beam waves and found that the hull's drift angle induced lateral motions such as sway, roll, and

* Corresponding author at: Maritime Engineering, University of Southampton, Boldrewood Campus, Southampton, SO16 7QF, Hampshire, UK.
** Corresponding author.
E-mail addresses: Yifu.Zhang@soton.ac.uk (Y. Zhang), hectorruben.diaz@ulpgc.es (H.R. Díaz-Ojeda).

yaw in direct head waves, intensifying with an increase in drift angle, while having minimal impact on surge, heave, and pitch. Choi et al. (2019) reported findings from oblique tests in regular waves on a fixed KCS model, measuring the average lateral force and yaw moment. Experimental methods can yield crucial data for validating CFD codes and understanding the physics of ship manoeuvring (Turnock et al., 2024). However, these tests are expensive, time-intensive, and subject to uncertainties, often demanding high-specification facilities, precise ship models, and skilled technicians (Zhang, 2023).

Numerous numerical approaches have been developed to analyse ship manoeuvring in waves. Prominent among these are mean wave force methods, two-time scale methods, unified methods and CFD based direct simulation methods (ITTC, 2021). The mean wave force method integrates only the mean wave force into the existing calm water prediction models (Hirano et al., 1980). This approach with the assumption of a slender ship, is theoretically sound (Nonaka, 1990). It has been widely applied by researchers like Papanikolaou et al. (2016), Yasukawa et al. (2017), Tello Ruiz et al. (2019) and Aung and Umeda (2020) to assess different manoeuvring motions in both regular and irregular waves. The main limitation of this method is its inability to account for wave-induced motions like heave, pitch, and roll during manoeuvring. The two-time scale method, proposed by Yasukawa (2006) and Skejic and Faltinsen (2008), categorizes the fundamental motion equations into two groups: (a) low-frequency manoeuvring motions and (b) high-frequency wave-induced motions. It solves the equations for both manoeuvring and seakeeping by accounting for their interaction in time-domain. Yasukawa and Nakayama (2009) used this method to compute both manoeuvring and wave-induced motions and validated their model by comparing the simulation outputs with data from free-running wave tests using a scale model of the S175 container ship. Seo and Kim (2011), Zhang and Zou (2016) and Lee and Kim (2020) employed a coupling method using the time-domain Rankine panel method to integrate seakeeping and manoeuvring quantities. This method performed seakeeping analysis based on the ship's instantaneous velocity and the wave's incident direction, integrating the resulting wave-induced motions and forces into the manoeuvring equation of motion. The hybrid two-time scale model using RANS for low-frequency manoeuvring motions and BEM (Boundary Element Method) for high-frequency seakeeping challenges was also developed (Piro et al., 2020; White, 2020; White et al., 2022). This model excelled in turning circle simulations of DTC and KCS models in both calm and wavy conditions, effectively predicting ship manoeuvring and seakeeping performance. The unified method, a type of direct simulation approach, integrates the 6DOF motion equations by combining unified manoeuvrability and seakeeping solutions with wave-induced Froude–Krylov, radiation, and diffraction forces. This method delivers precise and comprehensive predictions of ship manoeuvring and seakeeping performance in wave conditions (Subramanian and Beck, 2015; Paramesh and Rajendran, 2021; Suzuki et al., 2021). Although the aforementioned methods can effectively predict ship manoeuvring motions in waves, they are significantly limited by their inability to capture nonlinear phenomena, instantaneous free surfaces, and detailed local flow fields. In comparison, the CFD based direct simulation methods using free-running simulations (e.g.turning and zigzag manoeuvres) can provide better ship manoeuvrability in waves assessment because it includes the viscous and rotational effects, and it can capture the interaction between the hull, propeller, rudder and waves (Kim et al., 2021). Carrica et al. (2013) conducted numerical simulations of ship manoeuvring in waves using a simplified body force propeller model and implemented an overset grid to manage ship motions and rudder steering. The primary discrepancy between the CFD simulations and experimental results is likely attributable to the simplistic nature of the propeller model. Shen and Korpus (2015) employed a dynamic overset grid technique and conducted simulations of a free-running ship ONRT model navigating head and quartering waves while maintaining course control, showing good agreement with experimental validation data. Wang and Wan

(2016), Wang and Wan (2018) and Wang et al. (2018) employed naoe-FOAM-SJTU to simulate the free-running course-keeping challenge, along with zigzag and turning circle manoeuvres under various wave conditions for a fully appended twin-screw ship (ONR Tumblehome). The trajectory and main parameters demonstrated good comparison with experimental data. Kim et al. (2021) performed a fully nonlinear unsteady RANS simulation to forecast the manoeuvring behaviour of a KRISO Container ship (KCS) model under various wave conditions. The simulation incorporated a course-keeping and manoeuvring control module based on a feedback control system, which controlled rudder deflection according to established manoeuvring procedures.

Direct CFD simulation can provide accurate prediction for ship manoeuvring in waves with the highest fluid dynamic fidelity. However, this kind of methods, particularly for full 6DOF manoeuvring simulations in waves with discretized propeller and rudder models, require significant computational effort because of very small time step and finely refined grids. Besides, the 6DOF overset method is mostly useful for studying a specific manoeuvre and proof of concept for the 6DOF solver. Consequently, the practical use of this approach is still very limited for initial ship design. In addition, numerical approaches of captive manoeuvring tests (the planar mechanic mechanism (PMM) test or circular motion test (CMT)) can also be employed for ship manoeuvring predictions. Simonsen et al. (2012) conducted KCS PMM model test and compared the static drift test results between the experiment and a commercial CFD solver and good agreement is found between EFD and CFD. Sung and Park (2015) conducted RANS-based virtual captive model tests with StarCCM+ to estimate bare hull manoeuvring coefficients, showing good alignment with PMM test data. Islam and Soares (2018) carried out static drift, pure sway and pure yaw simulation using OpenFOAM and results were compared with experimental data. Du et al. (2022) investigated the manoeuvring motion of the KVLCC2 hull using virtual captive model tests that included rudder force and open water tests. Zhu et al. (2022) conducted numerical PMM tests with open source code and generated a complete list of manoeuvring coefficients for the bare hull.

The literature review reveals that while significant progress has been made in predicting ship manoeuvring in waves, several challenges persist, underscoring the need for improved methodologies. Experimental methods remain a standard for validating numerical models and understanding the fundamental physics involved. However, the high costs of these methods, due to the need for advanced facilities and detailed scale models, limit their widespread use. Various approaches have been developed on the numerical front, each with its limitations. Mean wave force methods, two-time scale methods, and unified methods struggle to capture complex nonlinear effects and dynamic free surface interactions accurately. Although CFD-based direct simulation methods offer a potential solution by addressing these nonlinearities, they come at the expense of increased computational demands, necessitated by small time steps and highly refined mesh requirements. Furthermore, most numerical models, particularly those simulating captive manoeuvring tests, typically focus on configurations such as bare hulls or hulls with rudders in calm water and often overlook critical dynamics such as those involving rotating propellers and actual wave conditions. Additionally, few studies have investigated the combined impact of drift and rudder angles on hull–propeller–rudder interactions under varying wave conditions and different propeller thrust loads. Our study aims to bridge these gaps by developing a more efficient and comprehensive numerical method that extends beyond traditional modelling limitations to include interactions with waves and propeller dynamics, thereby offering a more accurate and practical tool for studying ship manoeuvring in real sea states.

This paper presents a cost-effective numerical method for simulating a fully appended KRISO Container Ship (KCS) in waves with varying propeller thrust loading conditions, focusing on static drift, static rudder, and combined drift-rudder scenarios to approximate the quasi-static phases of real ship manoeuvres. This targeted approach

avoids the need to model full transient manoeuvres, significantly reducing computational costs. By analysing fixed-angle simulations, we can precisely examine the fluid dynamics around the hull and rudder. More crucially, this method allows us to develop Reduced Order Models (ROMs) based on hydrodynamic coefficients from the measured forces at various rudder and drift angles, paving the way for a real-time ship manoeuvrability simulator. Real-time modelling is impractical for complete 6DOF simulations, but by utilizing a finite set of angles, we gather sufficient data to create effective ROMs without excessive costs. Furthermore, the simulation under static drift and rudder conditions allows for direct validation and contributes to the future validation process of the actual dynamic manoeuvring models and simulations. The investigation of drift's influence on fully appended vessels also helps to gain a better understanding of the effects of wind-assist devices on ship powering performance. Wind-assist systems can reduce the propeller-generated thrust and also create lateral forces on the hull, leading the ship to operate at an angle of drift. By examining these relationships, this research aids in the optimization of ship designs that harness wind assistance, thereby contributing to maritime decarbonization efforts.

The remainder of this paper is organized as follows. The methodology utilized for the numerical analysis in this study is outlined in Section 2, which includes a concise overview of the governing equations, the applied RANS-CFD solver, numerical propeller modelling, and the coupling between RANS and body force model. Section 3 provides a detailed case study, introducing the hull geometry, establishing the coordinate systems used for drift computations, and elaborating on the specifics of the computational simulations conducted. The process of generating grids and conducting numerical validations is detailed in Section 4. Subsequently, Section 5 presents the numerical results and comparison is made with experimental data. The paper concludes in Section 6 with a summary of the key findings and implications of the research.

2. Numerical methodology

2.1. Governing equations

The dynamics of fluid movement around the fully appended KCS can be simulated by employing the unsteady Reynolds Averaged Navier–Stokes (RANS) equations. When addressing unsteady incompressible flows, the continuity and momentum equations are reformulated in tensor notation within Cartesian coordinates (Ferziger et al., 2019). These equations are presented as follows:

$$\frac{\partial \overline{u}_i}{\partial x_i} = 0 \tag{1}$$

$$\rho \frac{\partial \overline{u}_i}{\partial t} + \rho \frac{\partial \overline{u}_i \overline{u}_j}{\partial x_j} = -\frac{\partial \overline{p}}{\partial x_i} + \frac{\partial}{\partial x_j} \left[\mu \left(\frac{\partial \overline{u}_i}{\partial x_j} + \frac{\partial \overline{u}_j}{\partial x_i} \right) \right] - \rho \overline{u_i' u_j'} + \overline{F}_i \tag{2}$$

In this formulation, $\overline{u}$ and $\overline{p}$ represent the mean velocity and pressure fields respectively, while ρ denotes the fluid density, and μ is the dynamic viscosity. To address the Reynolds stress $\overline{u_i' u_j'}$, the Shear Stress Transport (SST) $k - \omega$ turbulence model is utilized to ensure turbulence closure. This model, initially developed by Menter (1994), includes a blending function that facilitates a seamless transition between the $k - \omega$ and $k - \epsilon$ models, optimizing the model's accuracy across different flow regimes. The SST $k - \omega$ model has been further updated by Menter et al. (2003), making it highly effective for predicting the hydrodynamic performance of ships, particularly in wave-induced conditions. Based on Menter et al. (2003), the equation for eddy viscosity (ν_T) can be written as Eq. (3), which also includes equations for strain rate tensor magnitude (S) and rate of strain tensor (S_{ij}):

$$\nu_T = \frac{a_\omega k}{\max(a_\omega \omega, SF_2)} \qquad S = \sqrt{2S_{ij}S_{ij}} \qquad S_{ij} = \frac{1}{2} \left(\frac{\partial u_i}{\partial x_j} + \frac{\partial u_j}{\partial x_i} \right) \tag{3}$$

Besides, Eqs. (4) and (5) are two transport equations for kinetic energy (k) and specific dissipation rate (ω):

$$\frac{\partial k}{\partial t} + \frac{\partial (u_j k)}{\partial x_j} = P_k - \beta^* k\omega + \frac{\partial}{\partial x_j} \left((\nu + \sigma_k \nu_T) \frac{\partial k}{\partial x_j} \right) \tag{4}$$

$$\frac{\partial \omega}{\partial t} + \frac{\partial (u_j \omega)}{\partial x_j} = \frac{\gamma P_k}{\nu_T} - \beta \omega^2 + \frac{\partial}{\partial x_j} \left((\nu + \sigma_\omega \nu_T) \frac{\partial \omega}{\partial x_j} \right) + 2(1 - F_{k\omega}) \frac{\sigma_{\omega 2}}{\omega} \frac{\partial k}{\partial x_i} \frac{\partial \omega}{\partial x_i} \tag{5}$$

The constants are blended using the blending function $F_{k\omega 1}$ as shown in Eqs. (6) and (7):

$$\gamma = F_{k\omega}\gamma_{k\omega 1} + (1 - F_{k\omega})\gamma_{k\omega 2} \qquad \beta = F_{k\omega}\beta_{k\omega 1} + (1 - F_{k\omega})\beta_{k\omega 2} \tag{6}$$

$$\sigma_k = F_{k\omega}\sigma_{k\omega 1} + (1 - F_{k\omega})\sigma_{k\omega 2} \qquad \sigma_\omega = F_{k\omega}\sigma_{\omega 1} + (1 - F_{k\omega})\sigma_{\omega 2} \tag{7}$$

Based on the wall distance y, definitions of blending functions $F_{k\omega 1}$ and $F_{k\omega 2}$ are described in Eq. (8):

$$F_{k\omega 1} = \tanh \left(\min \left(\max \left(\frac{\sqrt{k}}{\beta^* \omega y}, \frac{500\nu}{y^2 \omega} \right), \frac{4\sigma_{\omega 2} k}{CD_{k\omega} y^2} \right)^4 \right)$$

$$F_{k\omega 2} = \tanh \left(\max \left(\frac{2\sqrt{k}}{\beta^* \omega y}, \frac{500\nu}{y^2 \omega} \right)^2 \right) \tag{8}$$

And equations for $CD_{k\omega}$ and production term P_k is defined in Eq. (9):

$$CD_{k\omega} = \max \left(2\rho\sigma_{\omega 2} \frac{1}{\omega} \frac{\partial k}{\partial x_i} \frac{\partial \omega}{\partial x_i}, 10^{-10} \right) \qquad P_k = \min \left(\tau_{ij} \frac{\partial u_i}{\partial x_j}, 10\beta^* k\omega \right) \tag{9}$$

Both robustness and accuracy of $SST k - \omega$ turbulent model have been validated in various studies and applications. Notably, this model was employed in 80 percent of the submissions at the 2010 Gothenburg workshop on numerical hydrodynamics (Larsson et al., 2013), underscoring its widespread acceptance and reliability in the field. Additionally, it has been successfully applied to simulate ship manoeuvring behaviours under drift conditions, as demonstrated in studies by Phillips et al. (2009), Zhang et al. (2021) and Zhang et al. (2022).

2.2. Applied RANS-CFD solver

The numerical solution of the governing equations is executed using the open-source RANS solver OpenFOAM version 7 (OpenFOAMFoundation, 2019). These unsteady RANS equations are discretized using the Finite Volume Method (FVM). During this discretization phase, the Euler scheme is applied for temporal discretization, while a second-order upwind scheme is adopted for the convection term to enhance accuracy. For spatial discretization, the Gauss linear scheme is used for gradients, and the Gauss linear corrected scheme is chosen for discretizing the Laplacian terms, which helps in maintaining numerical stability and accuracy.

In OpenFOAM, the interFoam solver is specifically utilized for simulating two-phase flows. This solver is adept at calculating the dynamic interactions between two immiscible fluids under the assumption that both are incompressible, such as water and air, making it particularly suitable for maritime applications involving complex fluid interfaces. For coupling pressure and velocity fields, the PIMPLE (Pressure-Implicit with Operator-Splitting Multi-Phase Explicit) algorithm is employed, which integrates the features of both PISO (Pressure Implicit with Splitting of Operators) and SIMPLE (Semi-Implicit Method for Pressure-Linked Equations) algorithms. This integration includes mechanisms for velocity correction and under-relaxation, which enhance the solver's capability to handle transient flow conditions effectively. The use of PIMPLE is particularly advantageous in scenarios like modelling ship stern flows, where unsteady fluid dynamics are critical.

The Volume of Fluid (VOF) method is employed to effectively capture the dynamics of the free surface and to model the interactions between the water and air interfaces. In the VOF method, the volume fraction, denoted by α, is central to understanding the phase distribution and is governed by the transport equation:

$$\frac{\partial \alpha}{\partial t} + \nabla \cdot (\alpha \mathbf{u}) = 0 \tag{10}$$

In this context, α quantifies the proportion of one phase in a two-phase flow, and $\mathbf{u}$ represents the velocity vector of the flow. A cell completely filled with water is indicated by a volume fraction $\alpha = 1$, whereas a cell filled with air has $\alpha = 0$. The interface between these two phases, or the free surface, is identified by cells having intermediate α values between 0 and 1. These cells contain a mixture of both air and water, and the distribution of α across the cells precisely tracks the location and configuration of the free surface.

2.3. Numerical propeller modelling

To achieve reliable manoeuvring performance of fully-appended ships in waves, accurate numerical modelling of propeller is essential. There are various numerical modelling approaches, for example, ranging from a basic actuator disc, in which the force is evenly distributed across the disc's radius following an ideal distribution, to a comprehensive panel code for the propeller where the force is derived from the pressure exerted on each individual panel (Molland et al., 2017). The choice of propeller numerical methods depends on the level of accuracy required and the computational resources available. In terms of numerical approaches for marine propeller modelling, the most commonly used techniques in CFD are the body force method and the fully discretized propeller approach. The two most widely adopted approaches for fully discretized propeller modelling are the sliding interface method and the dynamic overset grid method (Gatin et al., 2018), and both of them requires a high mesh resolution of propeller geometry and a smaller time step to resolve the fully transient propeller flow, which inevitably results in complex meshes, increased simulation time and high computational cost. In comparison, the body force model is relatively cost-effective and requires less computational resources when a detailed capture of the propeller flow is not essential, making it well suited for the current study, where simulations primarily concern the hull–propeller–rudder–wave interaction effect instead of directly focusing on propeller itself.

In body force model, the momentum imparted by the rotating propeller blades is introduced directly into the URANS momentum equations as an additional source of momentum or body force. Expressed in Cartesian coordinates, the URANS momentum equations indicate that the flow field, represented by $\bar{\mathbf{u}} = (u, v, w)$, is accelerated by the body force, which is denoted as $\bar{\mathbf{F}}_\mathbf{v} = (F_{vx}, F_{vy}, F_{vz})$. Therefore, the momentum equations that include this body force term can be articulated as follows:

$$\frac{\partial(\rho u)}{\partial t} + \nabla \cdot (\rho u \bar{u}) = -\frac{\partial p}{\partial x} + \frac{\partial \tau_{xx}}{\partial x} + \frac{\partial \tau_{yx}}{\partial y} + \frac{\partial \tau_{zx}}{\partial z} + \rho F_{vx}$$

$$\frac{\partial(\rho v)}{\partial t} + \nabla \cdot (\rho v \bar{u}) = -\frac{\partial p}{\partial y} + \frac{\partial \tau_{xy}}{\partial x} + \frac{\partial \tau_{yy}}{\partial y} + \frac{\partial \tau_{zy}}{\partial z} + \rho F_{vy} \tag{11}$$

$$\frac{\partial(\rho w)}{\partial t} + \nabla \cdot (\rho w \bar{u}) = -\frac{\partial p}{\partial z} + \frac{\partial \tau_{xz}}{\partial x} + \frac{\partial \tau_{yz}}{\partial y} + \frac{\partial \tau_{zz}}{\partial z} + \rho F_{vz}$$

In this paper, the body force model, Blade Element Momentum Theory (BEMt), is adopted for all cases. BEMt integrates axial momentum theory with 2D blade element theory, initially proposed by Burrill (1944). This theory is suitable for performing calculations on marine propellers under conditions close to their designed operational state. It relies on the lift and drag generated by an airfoil, where the angle of attack is determined by both the local pitch and the incidence of the incoming velocity which is determined by the propeller's rotation and the characteristics of the nominal wake. The integration of blade element theory with momentum theory is accomplished by aligning
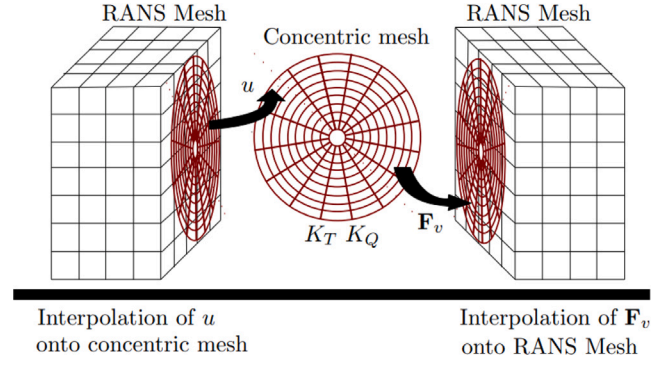

Fig. 1. Mapping of velocity and body force between RANS and concentric mesh (Windén, 2014).

their respective efficiency estimates. The Blade Element Momentum theory (BEMt) also presupposes prior knowledge of the lift and drag characteristics of the blade section. In this model, C_L (coefficient of lift) is estimated from the force balance of thrust from the previous iteration, while C_D (coefficient of drag) is derived by fitting a curve to an experimentally obtained $C_D - \alpha$ (drag coefficient vs. angle of attack) relationship. The application of BEMt in this paper adheres to the methodologies outlined by Molland et al. (2017) and a more detailed description of BEMt can be found in Zhang et al. (2024).

2.4. RANS-BEMt coupling

The coupling between the RANS solver and BEMt is achieved using a two-way coupling. Initially, the velocity derived from the RANS solution is utilized to generate a wakefield, which directly impacts how propeller thrust and torque are distributed within the propeller code. Subsequently, these propeller thrust and torque variations are reintroduced into the RANS domain, reflecting the shifts in velocity and pressure stemming from the propeller's presence. The mapping of velocity $\mathbf{u}$ and body force $\mathbf{F}_\mathbf{v}$ between RANS (hull–rudder) and concentric (propeller) meshes is illustrated in Fig. 1 and the equations coupling is also demonstrated in Fig. 2. In this study, the custom solver selfPropinterFoam is used to simulate all considered cases involving propeller modelling. A detailed description of selfPropinterFoam, which utilizes RANS-BEMt coupling, can be found in Windén (2021a,b). The effectiveness of this coupling method for hull–propeller–rudder system has been proven in previous studies such as Zhang et al. (2024), Windén (2021a), Molland et al. (2017), Badoe et al. (2015) and Phillips et al. (2009).

3. Case description

3.1. Fully appended KCS geometry

In this research, the KCS is selected as the subject vessel, due to its substantial background in both experimental and computational studies. As a modern container ship, the KCS provides a detailed understanding of fluid dynamics, making it an ideal model for both validating and verifying numerical models in the field of ocean engineering. This vessel's extensive use in prior research (SIMMAN (2008), SIMMAN (2014, 2020), Stern et al. (2011)) enhances its suitability as a benchmark model, facilitating a deeper exploration into the complexities of ship manoeuvring behaviour in wave conditions. The illustration of fully appended Tokyo model scale KCS geometry is shown in Fig. 3, including side view of fully appended KCS and its rudder profile. Table 1 provides the main particulars of the KCS, employing a model with a scale ratio $\lambda = 31.60$ ($L_{PP} = 7.2786$ m) for all numerical simulations in this analysis. This model aligns with the KCS model 1 from the 2015 Tokyo CFD workshop as described in Hino et al. (2020).

Table 1
Main particulars of KCS.

| Parameter	Full scale	Tokyo'15 model 1 scale	SOTON model scale
Scale ratio, λ	1	31.60	60.96
Length between perpendicular, L_{pp} (m)	230	7.2786	3.7729
Maximum beam of waterline, B_{WL} (m)	32.2	1.0190	0.53
Depth, D (m)	19	0.6013	0.282
Draft, T (m)	10.8	0.3418	0.1772
Displacement, ∇ (m³)	52030	1.6490	0.2297
Wetted surface area w/o rudder, S_W (m²)	9424	9.4379	2.5359
Froude Number, Fn	0.26	0.26	0.26
Design speed, U (m/s)	12.35	2.196	1.5818
Propeller diameter, D_P (m)	7.9	0.25	0.13
Propeller hub ratio, D_H/D_P	0.18	0.18	0.18
The number of propeller blades, Z	5	5	5
Propeller rotation direction (view from stern)	clockwise	clockwise	clockwise
Moment of Inertia, (K_{XX}/B)	0.4	0.4	0.4
Moment of Inertia, $(K_{yy}/L_{pp}, K_{ZZ}/L_{pp})$	0.25	0.25	0.25
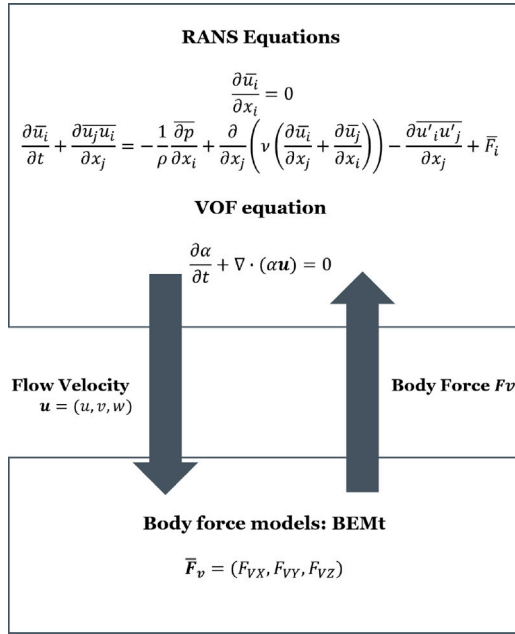
Fig. 2. Equations coupling between RANS and BEMt.

3.2. Coordinate systems used for computations

The simulation of a ship navigating under drift conditions necessitates employing two coordinate systems due to the misalignment of the ship's longitudinal and transverse axes with those of the computational domain. This study incorporates both the computational domain system and the ship-fixed system, adhering to the right-hand rule, as depicted in Fig. 4. Primarily, the calculations of hydrodynamic forces and moments are conducted within the ship-fixed coordinate system, designated as O-XYZ, unless specified otherwise. This system is defined with the x-axis directed toward the bow, the y-axis pointing starboard, and its origin located at mid-ship.

The drift angle of the ship, denoted as β, is considered positive when the ship's deviation is toward the starboard side. Similarly, the rudder angle, β_r, is defined as positive when the rudder is oriented to the starboard, aligning with the right side when facing forward. Besides, the ship's resistance is represented by R, while the lateral force exerted on the hull is denoted by F_Y, and the yaw moment by M_Z. Additionally, the rudder forces include D, which corresponds to the drag, and L, which represents the lift generated by the rudder. These forces are crucial for the ship's manoeuvrability and are calculated within the aforementioned ship-fixed coordinate system, as illustrated in Fig. 4.

3.3. Computational simulations

3.3.1. Simulation conditions

In this research, the fully appended Tokyo model scale KCS is subjected to simulations under three regular wave conditions. The study specifically explores three different drift angles, designated as $\beta = -10°$, $\beta = 0°$, and $\beta = +10°$. A range of static rudder angles is implemented for each of these drift conditions. Initially, the wave resistance tests are conducted for all cases using the KCS hull equipped with the rudder but without a propeller. These tests are carried out at the ship's design speed, with a Froude number (F_n) of 0.26 and a corresponding ship speed (U) of 2.196 m/s and the ship is free to heave and pitch. Following this, the study advances to perform a series of fixed RPM tests, applying RPM values of 900, 1200, and 1500 across the three wave conditions and the ship is fixed. These tests utilize the Blade Element Momentum theory (BEMt) for propeller modelling. The simulation conditions are detailed as follows:

- KCS at drift angle, $\beta = 0°$, with five static rudder angles, $\beta_r = -20°, -10°, 0°, 10°, 20°$.
- KCS at drift angle, $\beta = -10°$, with five static rudder angles, $\beta_r = -20°, -10°, 0°, 10°, 20°$.
- KCS at drift angle, $\beta = +10°$, with five static rudder angles, $\beta_r = -20°, -10°, 0°, 10°, 20°$.

3.3.2. Wave generation, damping and properties

The OpenFOAM v7 software suite employs its default wave generator for the creation of waves, utilizing the setWaves utility to incorporate specific wave models into the computational domain for case initialization. This process employs level sets to achieve second-order accuracy in wave modelling, as detailed by OpenFOAM Foundation (2023). Wave damping in our study was implemented using a runtime selectable source term, integrated through a new fvOption called verticalDamping. This feature applies a damping force directly to velocity field components aligned with gravity, specifically designed to dampen wave motion and prevent reflections at the outlet boundary. Additionally, the configuration of wave parameters within OpenFOAM is facilitated through the implementation of specific boundary conditions, as outlined in Table 3. For the wave simulations, three distinct lengths of head waves — designated as R1, R3, and R5 — are utilized, representing short, medium, and long wave conditions respectively. These wave parameters, including wavelength and wave amplitude, are scaled based on the wave condition specifics from case 2.10 of the 2015 Tokyo workshop (Hino et al., 2020). The scaling is conducted relative to the L_{pp} ratio, and comprehensive details of the wave properties are shown in Table 2.
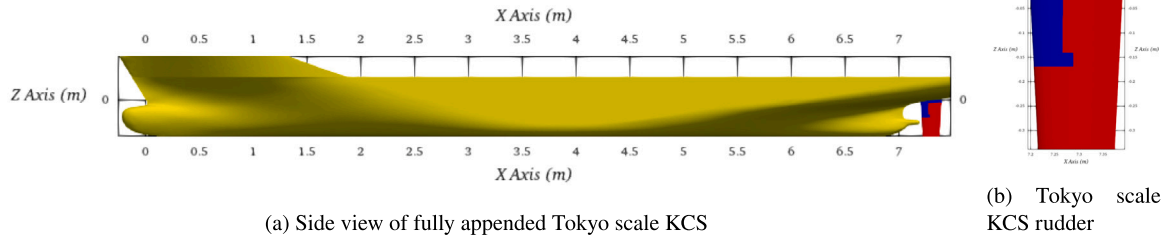
(b) Tokyo scale KCS rudder

(a) Side view of fully appended Tokyo scale KCS

Fig. 3. The geometry of Tokyo model scale KCS, hull (yellow), rudder skeg (blue), rudder blade (red) (Hino et al., 2020).

Table 2
Wave properties of three regular head waves.

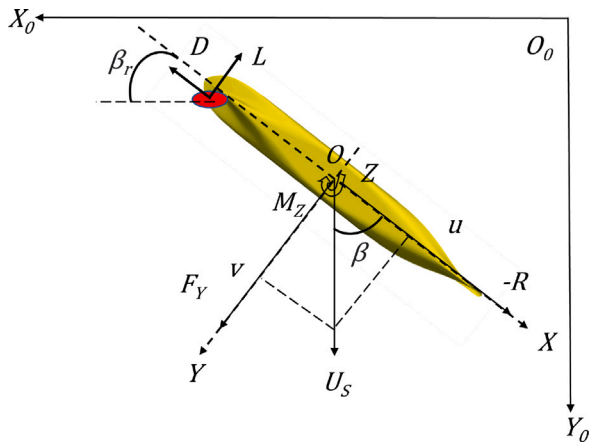| Parameter	Short wave R1	Medium wave R3	Long wave R5
Wave Type	Stokes 2nd Order	Stokes 2nd Order	Stokes 2nd Order
Non-Dimensional Wavelength (λ/L_{pp})	0.651	1.15	1.951
Wavelength (m)	4.735	8.368	14.197
Wave Frequency (Hz)	0.574	0.432	0.332
Wave Period (s)	1.741	2.315	3.015
Wave Speed (m/s)	2.719	3.615	4.708
Wave Number	1.327	0.751	0.443
Amplitude (m)	0.0372	0.0737	0.1175

Fig. 4. Coordinate systems and variables from bottom view.

3.3.3. Computational domain and boundary conditions

The computational domain for simulating the fully appended KCS in waves is configured in accordance with the CFD guidelines provided by ITTC (2014). The domain boundaries are defined with the inlet boundary located $1.0L_{pp}$ ahead of the KCS fore perpendicular (FP), and the outlet boundary $3.0L_{pp}$ behind the KCS aft perpendicular (AP). To reduce the influence of boundary walls on the simulation, the side boundaries are set $1.5L_{pp}$ away from the mid-ship position of the KCS hull. The lower boundary of the domain is set $1.5L_{pp}$ beneath the free surface, and the upper boundary is $1.0L_{pp}$ above it. A graphical representation of the computational domain's setup (from side and stern views) is depicted in Fig. 5.

The boundary conditions applied in this study are summarized in Table 3. The inlet boundary employs a fixed wave velocity and maintains a zero pressure gradient. The surfaces of the hull and rudder utilize a non-slip condition for velocity and a zero normal gradient for pressure. At the outlet boundary, the outlet phase mean velocity and zero gradient conditions are used for velocity and pressure respectively. Slip conditions are applied to the top, sides, and bottom of the domain boundaries. The volume force parameter (Fv) is employed to compute the propeller thrust and torque, facilitating propeller modelling through body forces without the need to mesh the propeller geometry directly.

3.3.4. Data collection and processing

The inclusion of wave dynamics in simulation models induces periodic fluctuations within the calculated outputs, such as ship resistance, throughout the converging period. As depicted in Fig. 6, the magnitude of these oscillations depends on the specific wave conditions encountered. Consequently, the analytical results in this investigation are derived by averaging the signal over several cycles. To ensure the precision of these calculated outputs, a minimum of five full cycles of the signal is employed to establish an average value. For example, the wave added resistance, denoted as R_{AW}, is calculated by averaging the total resistance signal under regular wave conditions R_T and subsequently deducting the calm water resistance R_{CW}, which corresponds to identical conditions of drift, rudder angles, and ship velocity, as derived from Zhang et al. (2024).

4. Grid generation

To generate appropriate meshes for simulating the fully appended KCS with drift and rudder angles in waves, the mesh utilities blockMesh and snappyHexMesh from OpenFOAM are used. Initially, the computational domain mesh, consisting of a hexahedral structured mesh, is constructed using blockMesh, which is also adopted for defining and refining the free surface region. Further enhancement of the mesh resolution around the KCS hull and rudder is achieved through the strategic deployment of four refinement boxes. These boxes facilitate the partitioning of cells in both horizontal and vertical orientations to refine the grid gradually, ensuring a heightened resolution of the structured mesh in critical areas. To ensure smooth transitions between areas with varying mesh densities, each refinement stage incorporates a gradual tapering of the mesh density. In addition, a smaller refinement box is specifically utilized to further refine the mesh in the stern region, encompassing the aft part of the KCS hull, the rudder, and the propeller area. To effectively capture the intricate dynamics of the boundary layer, the first cell height is determined based on a target value of $y^+ = 1$. The utility snappyHexMesh is then employed to add eight prism layers to the surfaces of the KCS hull and rudder, adhering to an expansion ratio of 1.2, recommended by ITTC (2014). It is important
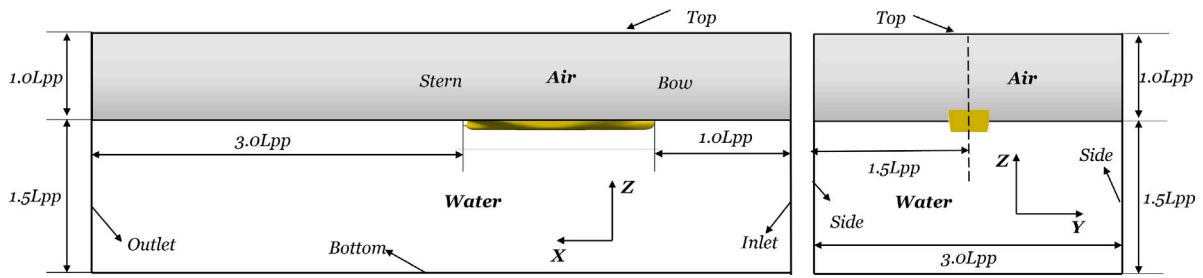
Fig. 5. Computational domain from side and stern views (zero drift angle case).

Table 3
The selected boundary conditions for regular wave simulations.

| Parameter	Inlet	Outlet	Top	Sides/Bottom	Hull/Rudder
U	waveVelocity	outletPhaseMeanVelocity	pressureInletOutletVelocity	symmetry	movingWallVelocity
p	fixedFluxPressure	zeroGradient	totalPressure	symmetry	fixedFluxPressure
k	fixedValue	inletOutlet	inletOutlet	symmetry	kqRWallFunction
ω	fixedValue	inletOutlet	inletOutlet	symmetry	omegaWallFunction
ν_t	fixedValue	zeroGradient	zeroGradient	symmetry	nutkRoughWallFunction
alpha	waveAlpha	variableHeightFlowRate	inletOutlet	symmetry	zeroGradient
volumeForce	fixedValue	fixedValue	fixedValue	symmetry	fixedValue
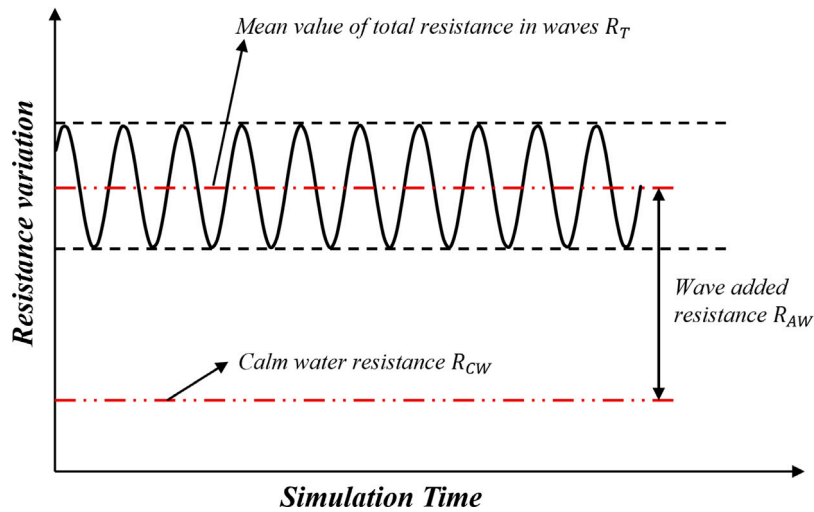
Fig. 6. Definition of measured quantities of added resistance in waves.

to note that in scenarios involving non-zero drift, modifications to the mesh generation procedures are necessary. The primary adaptation involves the rotation of the refinement boxes to align with the angle of drift, ensuring they are parallel to the longitudinal axis of the hull. This adjustment not only optimizes the mesh alignment relative to the flow but also reduces the overall mesh size and associated computational load. Table 4 displays the average values of y^+ for each component and the total mesh sizes for three different drift cases, derived under conditions where the KCS hull is subjected to drift with a rudder angle of zero degrees ($\beta_r = 0°$). However, variations in these values could occur in scenarios where the rudder angles differ, although such variations are generally minimal and do not significantly impact the overall mesh size.

Fig. 7 offers a comprehensive depiction of the grid distribution surrounding the KCS at a drift angle of 0°and a rudder angle of 0°, observed from the side view (XZ plane at the symmetry boundary) and the bow view (YZ plane at amidship). This representation distinctly illustrates the configuration of the previously mentioned refinement boxes. Furthermore, detailed views of the discretized computational domain adjacent to the stern and the bow are presented in Fig. 7(c) and Fig. 7(d), respectively.

Table 4
Average y^+ and total mesh size for different drift cases.

Parameter	$\beta = -10°$	$\beta = 0°$	$\beta = +10°$
y^+ of hull	1.13	1.05	1.13
y^+ of rudder blade	0.33	0.42	0.34
y^+ of rudder skeg	0.40	0.59	0.39
Total mesh size (million)	15.37	16.25	15.32

4.1. Validation and verification

4.1.1. Mesh and timestep

To ensure the reliability of numerical simulations, a validation and verification process is conducted on the KCS model moving straight ahead (zero drift angle $\beta = 0°$) with no rudder deflection($\beta_r = 0°$), operating at the ship design Froude number (0.26) in short wave R1 conditions ($\lambda/L_{pp} = 0.651$), allowing for heave and pitch movements. This setup corresponds to Case 2.1 of the KCS from the 2015 Tokyo Computational Fluid Dynamics (CFD) Workshop, albeit at different model scales. A detailed analysis is performed to evaluate the impact of grid spacing and time step on the simulation results, utilizing
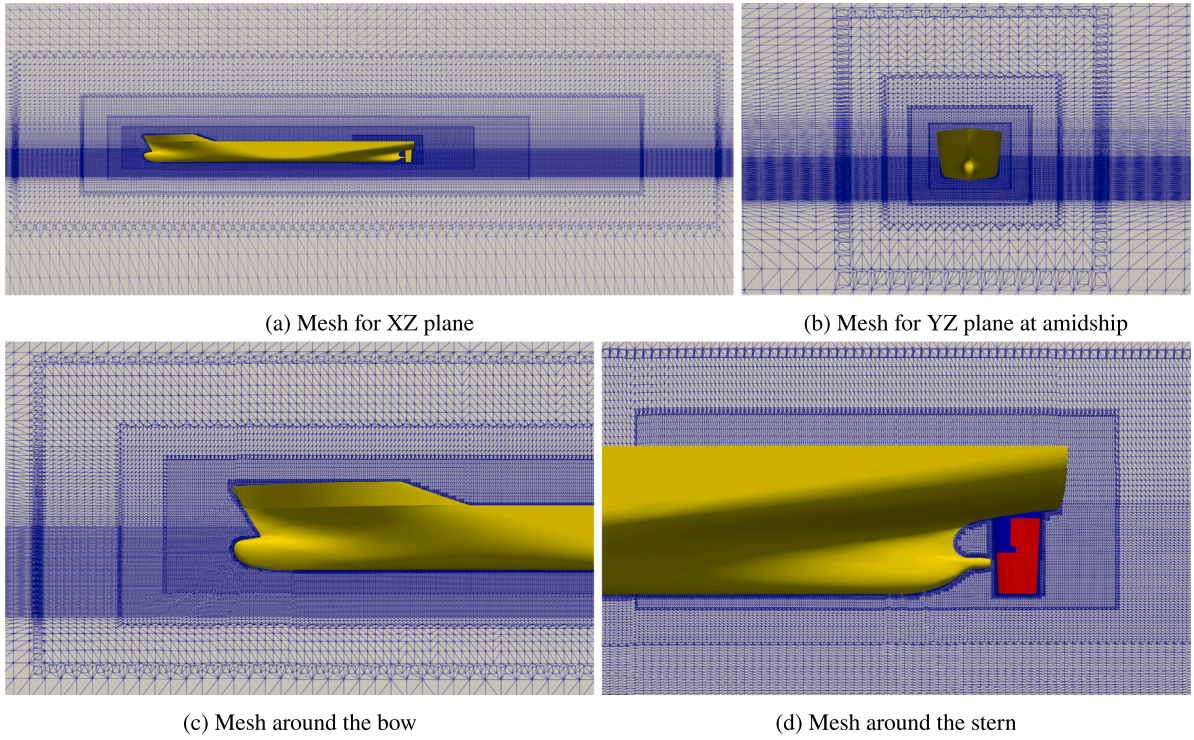
(a) Mesh for XZ plane

(b) Mesh for YZ plane at amidship

(c) Mesh around the bow

(d) Mesh around the stern

Fig. 7. The detailed mesh distribution around 0°drift KCS with 0°rudder.

methodologies derived from the studies by Stern et al. (2001) and ITTC (2017).

To evaluate grid sensitivity, three grids, Mesh 1, Mesh 2, and Mesh 3, are constructed using a structured background mesh with a uniform refinement factor of 1.1 across the same geometry. Table 5 details the grid configuration in the x, y, and z directions, along with total mesh sizes, time steps, simulation durations, and computational expenses. Table 6 displays the total resistance coefficients in short wave R1 ($\lambda/L_{pp} = 0.651$) using these different grid configurations and the computed results are compared with experimental data derived from Hino et al. (2020). As the CFD ($L_{pp} = 7.2786$ m) and EFD ($L_{pp} = 6.0702$ m) results are obtained using two different model scales' KCS, thus the standard scaling approach is used to fit and scale the total resistance. The used standard scaling approach is based on the following Eq. (12):

$$C_{T1} - C_{F1} = C_{T2} - C_{F2} \qquad C_F = \frac{0.075}{(\log_{10} Re - 2)^2} \qquad Re = \frac{u \cdot L_{PP}}{\nu} \quad (12)$$

Where C_T is the total resistance coefficient and C_F is the frictional resistance coefficient, which is derived by the ITTC-1957 formula. Re is the Reynolds number, u is the ship velocity in metres per second (m/s), L_{PP} is the length between perpendiculars, and ν is the kinematic viscosity.

Additionally, Table 7 documents the numerical uncertainties associated with the KCS total resistance coefficient in short wave R1, confirming the reliability of the simulation outcomes. Meanwhile, a time step sensitivity analysis is conducted using three different time steps, $\Delta t_1 = 0.0005$ s, $\Delta t_2 = 0.001$ s, and $\Delta t_3 = 0.002$ s on Mesh 3, and details are summarized in Table 5. As illustrated in Fig. 8(b), employing a smaller time step does not lead to significant changes or improvements in the outcomes, thus validating the time step sensitivity study. Given the considerable rise in computational demands when using finer grids and smaller time steps, Mesh 3 and a time step of $\Delta t_3 = 0.002$ s are chosen for all subsequent calculations. Moreover, Fig. 9 showcases the hydrodynamic pressure distribution on the free surface with different drift angles in three head waves, which displays adequate resolution with the chosen mesh density and time step.

4.1.2. Propeller open water performance

The performance of the BEMt propeller model in open water condition is evaluated to ensure the accuracy of the body force model used in this study. Table 8 and Fig. 10(a) display the open water performance results of the KCS propeller operating at a straight-ahead condition ($\beta = 0°$) as predicted by the BEMt model, alongside a comparison with experimental data sourced from Hino et al. (2020). The definitions for the propeller thrust and torque coefficients, open water efficiency, and advance ratio are provided in Eqs. (13) and (14), respectively.

$$K_T = \frac{T}{\rho n^2 D^4} \qquad K_Q = \frac{Q}{\rho n^2 D^5} \qquad (13)$$

$$\eta_o = \frac{K_T}{K_Q} \times \frac{J}{2\pi} \qquad J = \frac{U}{n \times D} \qquad (14)$$

where T and Q are the calculated propeller thrust and torque, J is the advance ratio, n refers to the number of revolutions and D is the propeller diameter, ρ is the density of water.

Overall, the propeller force predictions made by the BEMt model are in good alignment with experimental results. The most accurate predictions occur within the advance coefficient range of $0.4 < J < 0.8$, which encompasses all the rpm values examined in this study. Despite the propeller geometry being simplified to basic distributions of pitch and chord, the BEMt model successfully replicates the trend of open water performance curves across varying propeller advance ratios.

In addition, to verify the reliability of the BEMt model under oblique conditions, it is employed to model the effective wake of the KCS propeller when subjected to a uniform and oblique flow (drift angle $\beta = 10°$) and the computed open water results are shown in Table 8. The resulting propeller open water performance curves in oblique flow are then compared with those from straight-ahead conditions, as depicted in Fig. 10(b). Here, K_T, $10K_Q$, and η_0 are plotted against the advance ratio J, as specified in Eq. (6). However, the actual advance ratio J_i used in both models is defined as follows:

$$J_i = \frac{U \times \cos\beta}{n \times D} \qquad (15)$$

β represents the drift angle, set at 10°. Consistency in the rotational speed n across both non-yawed and yawed conditions results in

(a) Different meshes with the same Timestep Δt_3
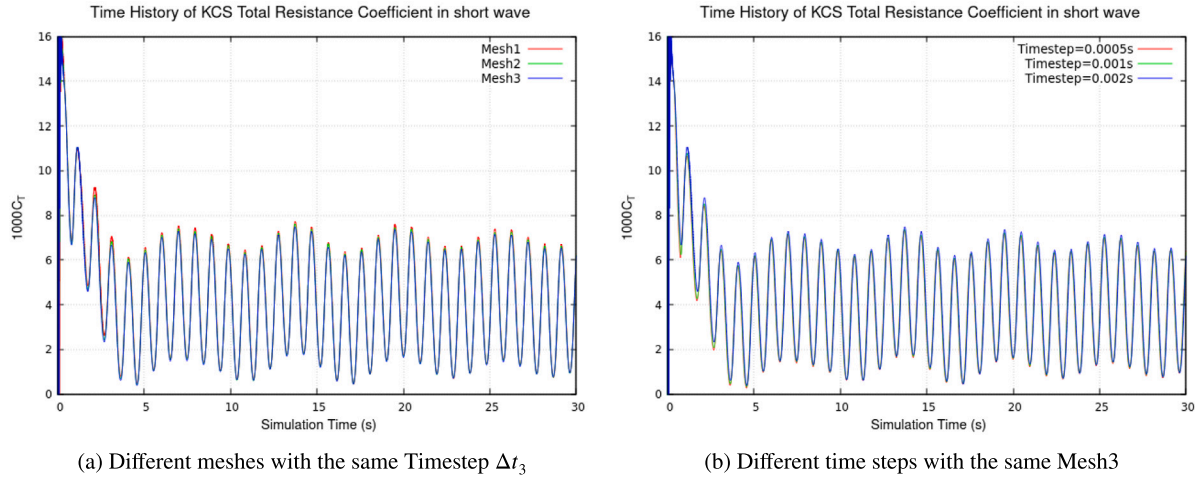
(b) Different time steps with the same Mesh3

Fig. 8. Time history of KCS total resistance coefficient in short wave R1 for Mesh and Timestep sensitivity study.

(a) $\beta = 0°$, $\beta_r = 0°$, short wave R1

(b) $\beta = 0°$, $\beta_r = 0°$, medium wave R3

(c) $\beta = 0°$, $\beta_r = 0°$, long wave R5

(d) $\beta = +10°$, $\beta_r = 0°$, short wave R1

(e) $\beta = +10°$, $\beta_r = 0°$, medium wave R3

(f) $\beta = +10°$, $\beta_r = 0°$, long wave R5

(g) $\beta = -10°$, $\beta_r = 0°$, short wave R1

(h) $\beta = -10°$, $\beta_r = 0°$, medium wave R3

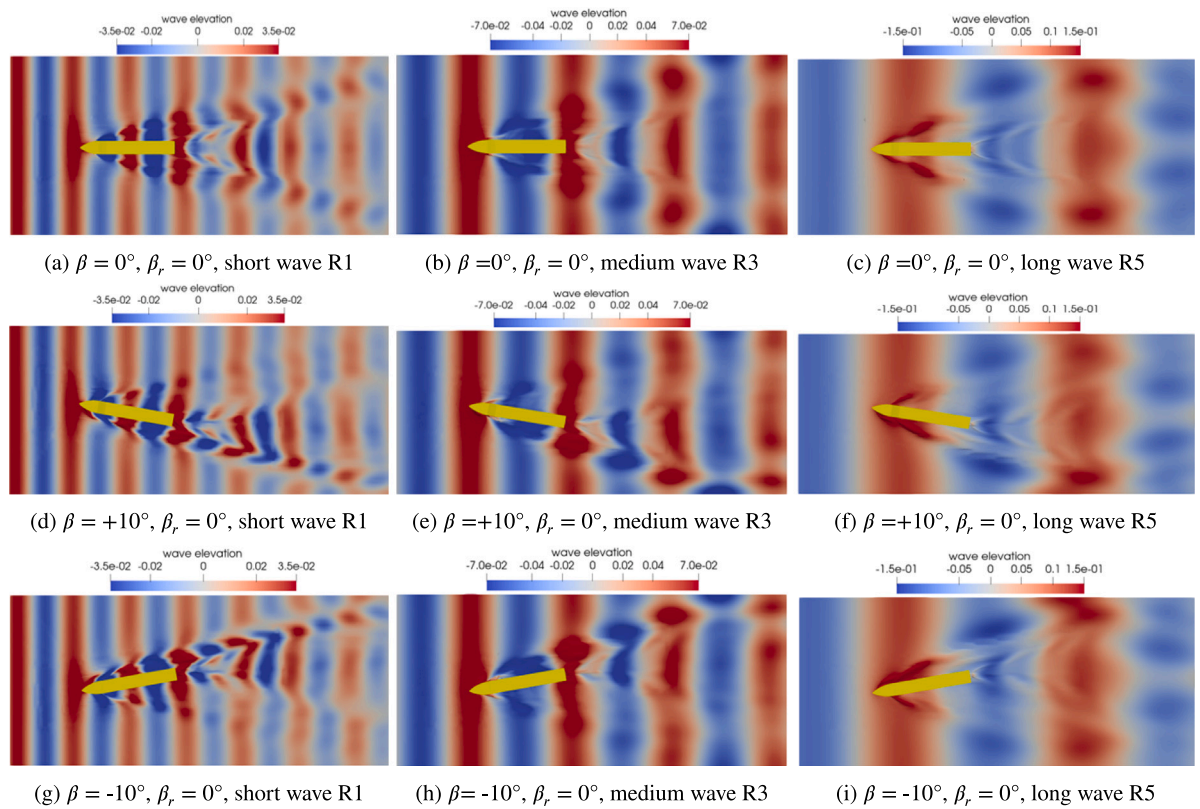(i) $\beta = -10°$, $\beta_r = 0°$, long wave R5

Fig. 9. Hydrodynamic pressure distribution on the free surface with different drift angles in three head waves.

Table 5
Computational system details for Mesh and Timestep sensitivity study.

Parameter	Mesh			Timestep (Δt)		
	1	2	3	1	2	3
blockMesh refinement	$133 \times 31 \times 48$	$121 \times 28 \times 44$	$110 \times 26 \times 40$	$110 \times 26 \times 40$	$110 \times 26 \times 40$	$110 \times 26 \times 40$
Total cell numbers (M)	26.3	20.5	16.3	16.3	16.3	16.3
Time step (s)	0.002	0.002	0.002	0.0005	0.001	0.002
Simulation Time (s)	30	30	30	30	30	30
Computational cost (hrs)	90–95	70–75	50–55	210–215	105–110	50–55
Computing system	Iridis 5 Linux Cluster, University of Southampton HPC Facility					
CPUs	Two nodes, 40 cores/node, 192GB DDR4 memory					
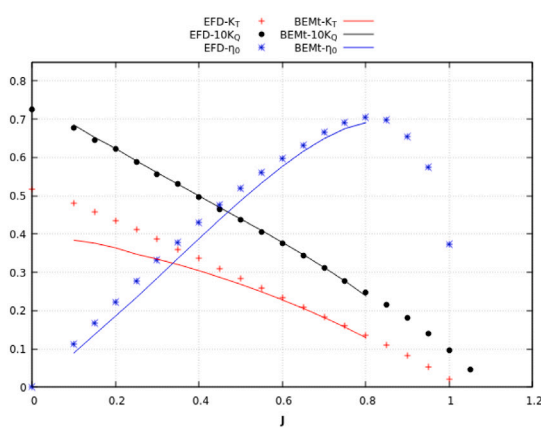
(a) Open water curve predicted by BEMt
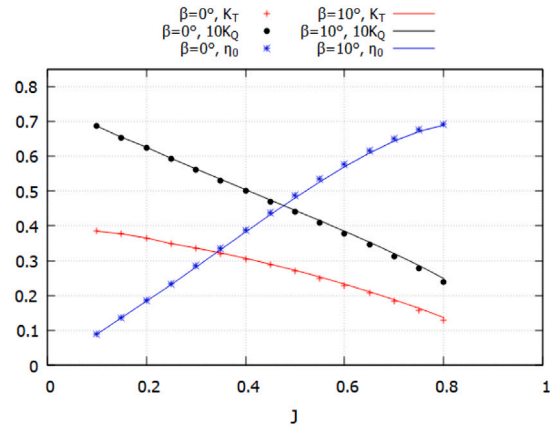
(b) Open water curve in oblique flow predicted by BEMt

Fig. 10. Open water performance of the KCS propeller predicted by BEMt and compared with EFD from Hino et al. (2020).

Table 6
Total resistance coefficients in short wave R1 ($\lambda/L_{pp} = 0.651$) of different grids.

Case	Timestep	$C_T/10^{-3}$	Diff.
Mesh1	$\Delta t_3 = 0.002$ s	3.933	−0.93%
Mesh2	$\Delta t_3 = 0.002$ s	3.915	−1.39%
Mesh3	$\Delta t_3 = 0.002$ s	3.891	−1.99%
EFD (Hino et al., 2020)	–	3.970	–

Table 7
The numerical uncertainties of resistance coefficients of different grids.

Parameter	r_G	R_G	Convergence conditions	C_G	U_{SN} (%D)	E(%D)
Grid	1.1	0.75	monotonic convergence	1.59	2.56	0.93

Table 8
Propeller open water results derived from BEMt and comparison with experimental results.

J	CFD($\beta = 0°$)			EFD (Hino et al., 2020)			CFD ($\beta = 10°$)		
	K_T	$10K_Q$	η_0	K_T	$10K_Q$	η_0	K_T	K_Q	η_0
0.10	0.3841	0.6851	0.0892	0.482	0.677	0.113	0.3843	0.6861	0.0878
0.15	0.3761	0.6527	0.1376	0.458	0.646	0.169	0.3765	0.6541	0.1353
0.20	0.3641	0.6236	0.1859	0.435	0.622	0.223	0.3648	0.6255	0.1828
0.25	0.3477	0.5912	0.2340	0.412	0.589	0.278	0.3486	0.5935	0.2301
0.30	0.3346	0.5604	0.2851	0.387	0.557	0.332	0.3359	0.5632	0.2804
0.35	0.3206	0.5304	0.3367	0.361	0.531	0.379	0.3222	0.5336	0.3312
0.40	0.3046	0.5002	0.3877	0.336	0.497	0.431	0.3066	0.5037	0.3816
0.45	0.2874	0.4698	0.4382	0.310	0.466	0.477	0.2898	0.4739	0.4313
0.50	0.2691	0.4398	0.4870	0.285	0.437	0.519	0.2720	0.4443	0.4797
0.55	0.2497	0.4098	0.5333	0.259	0.405	0.561	0.2530	0.4148	0.5258
0.60	0.2284	0.3782	0.5767	0.235	0.376	0.597	0.2323	0.3839	0.5691
0.65	0.2063	0.3464	0.6159	0.209	0.343	0.631	0.2107	0.3527	0.6085
0.70	0.1823	0.3128	0.6494	0.185	0.311	0.665	0.1876	0.3202	0.6428
0.75	0.1571	0.2775	0.6755	0.161	0.278	0.691	0.1629	0.2857	0.6704
0.80	0.1296	0.2387	0.6912	0.137	0.247	0.705	0.1364	0.2484	0.6886

$J_i \neq J$. Comparative analysis between the 0°and 10°scenarios shows a small divergence in results, attributable to the cosine of 10°being approximately 0.985, reflecting a minor deviation, nearly 99%, from the inflow velocity in a straight-ahead condition. Fig. 10(b) illustrates that the open water performance curves at a 10°drift angle closely resemble those in straight-ahead conditions. However, notable differences include an upward shift in the propeller thrust and torque coefficients and a downward shift in open water efficiency within the range of $0.35 < J < 0.8$, evident in the Blade Element Momentum theory (BEMt), underscoring the subtle impact of the drift angle on propeller performance.

5. Results

5.1. Hull–rudder interaction in waves

The plot shown in Fig. 11 displays the total longitudinal force coefficients of the straight-ahead KCS bare hull, which is the sum of pressure and viscous force coefficients in the x-direction over time for three different regular wave conditions. The mean value is computed by averaging crest or trough values from multiple cycles of converging oscillation periods to determine the total ship resistance coefficients in head waves; for instance, the value of C_T in long wavelength R5 is calculated by taking the mean of the signal from trough values at around t = 5 s to trough values approximately t = 20 s, as illustrated on the blue line from Fig. 11.

5.1.1. Drift influence on hull forces in waves
  • Total resistance, side force and yaw moment

Fig. 12 displays the total ship resistance C_T of straight-ahead KCS in regular waves, and comparisons are made with experimental data of Southampton model scale KCS. Experiments were conducted in Boldrewood Towing Tank at the University of Southampton in September 2022 and the SOTON KCS model was free to heave and pitch in regular waves tests and these tests were conducted at the ship's design speed with Froude number $Fn = 0.26$. While a comprehensive introduction of the EFD study is beyond the scope of this study, the detailed setup and experiments can be found in Bowker et al. (2023). The main particulars of the SOTON KCS model are presented in Table 1 and the Boldrewood towing tank dimensions are 138 m in length, 6 m in width and 3.5 m in depth. Since the CFD and EFD results were derived using two different model scales of KCS, the standard scaling approach is used to fit and scale the total resistance in waves from the SOTON scale to the Tokyo scale using the equation of $Ct_{Tokyo} - Cf_{Tokyo} = Ct_{Soton} - Cf_{Soton}$. Overall, it is evident that ship resistance increases as the wavelength increases. This is due to the higher speed over the hull in scenarios with higher wavelengths, resulting in a higher pressure force component: the values of C_T in R5 are approximately 1.3 times those in R1. CFD calculations exhibit the same variation trend as EFD data, although there are still deviations, especially in medium and long wave cases, approximately 7.3% and 10.1% in R3 and R5, respectively, at zero rudder angle. In addition to using an all-movable rudder in EFD, which can produce higher rudder drag in contrast to the semi-balanced rudder adopted in CFD simulations, another possible explanation for the observed discrepancy is that the fluctuating water pressure induced by the wave motion contributes to additional drag force on the rudder, and this effect is likely to be more significant in medium and long
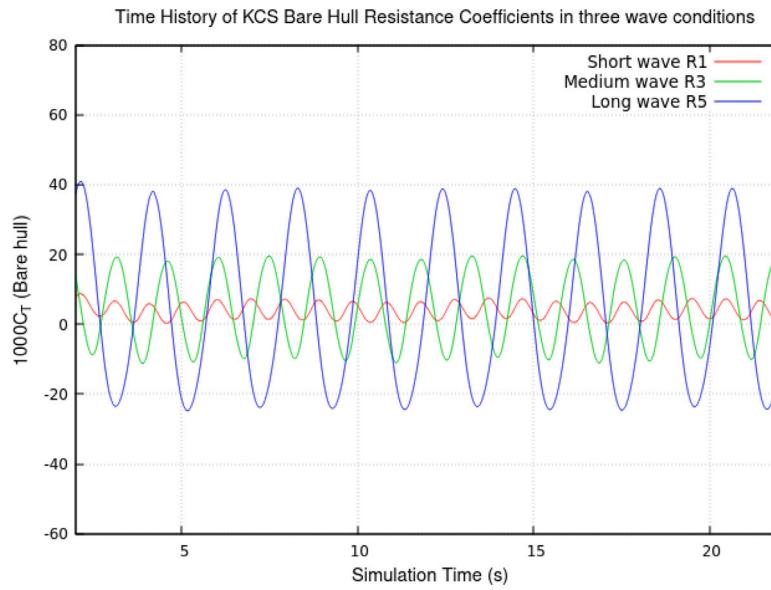
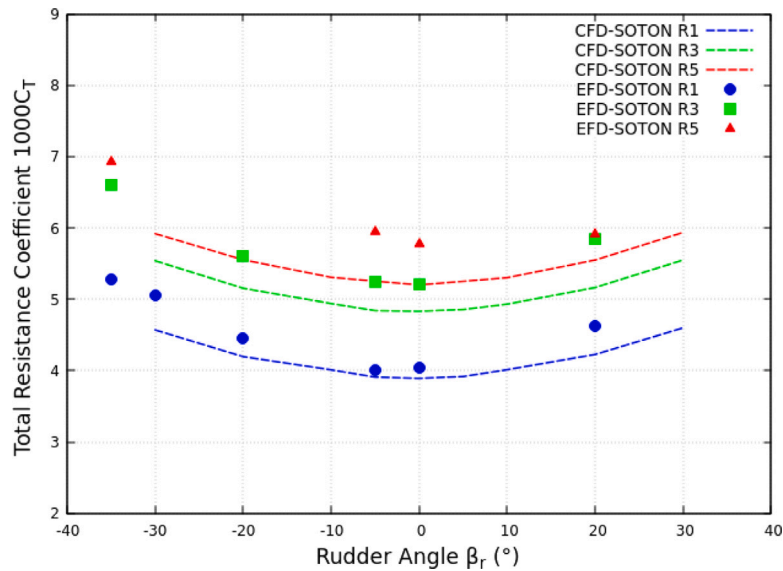**Fig. 11.** Time history of zero drift KCS bare hull resistance coefficients in three wave conditions.

Fig. 12. Comparison of CFD and EFD data for zero drift KCS total resistance coefficient C_T in R1, R3, R5 regular waves.

wave conditions than short wave. Table 9 lists the values of C_T in heading waves for drift KCS. The same phenomena can be found in non-zero drift scenarios: longer wavelength leads to higher drag forces. It is interesting to note the applied non-zero drift angles weaken this increasing tendency: the C_T ratio between R5 and R1 is around 1.2, while it is 1.3 in zero drift cases. Overall the trend of KCS drag at non-zero drift angles in the regular waves is similar to that of calm water: the maximum C_T occurs at $\beta_r = +20°$ for $+10°$ drift KCS while at $\beta_r = -20°$ when $-10°$ drift angle is employed.

The non-dimensionalized side force coefficients encountered by KCS in three waves are displayed in Table 10. In terms of different wave conditions, the highest lateral force is found at medium wave R3 for all drift cases, although differences in F'_Y are relatively tiny for three wavelengths' cases. The employed non-zero drift angle tends to shift the side force curve: a positive drift angle results in an upward shift, while a negative one leads to a downward tendency.

Table 10 also includes the non-dimensionalized yaw moment coefficients experienced by drift KCS in waves. In contrast to side force,

Table 9
Total ship resistance coefficients $1000C_T$ in head waves R1, R3 and R5 for KCS at non-zero drift angle: $\beta = +10°$, $-10°$.

$\beta = +10°$	rudder angle β_r (°)	R1	R3	R5
	−20	5.309	6.078	6.527
	−10	5.040	5.780	6.243
	0	4.906	5.643	6.122
	10	5.186	5.932	6.428
	20	5.707	6.447	6.940
$\beta = -10°$	rudder angle β_r (°)	R1	R3	R5
	−20	5.710	6.448	6.940
	−10	5.225	5.941	6.458
	0	4.922	5.650	6.142
	10	5.047	5.787	6.271
	20	5.331	6.075	6.547

Table 10
Non-dimensionalized side force and yaw moment coefficients experienced by KCS in head waves.

Drift angle	Rudder angle	$1000F_Y'$			$1000M_Z'$		
		R1	R3	R5	R1	R3	R5
$\beta = 0°$	$\beta_r = -30°$	−0.419	−0.443	−0.433	−0.0282	−0.0283	−0.0292
$\beta = 0°$	$\beta_r = -20°$	−0.351	−0.381	−0.386	−0.0228	−0.0230	−0.0254
$\beta = 0°$	$\beta_r = -10°$	−0.180	−0.197	−0.192	−0.0138	−0.0133	−0.0156
$\beta = 0°$	$\beta_r = -5°$	−0.122	−0.131	–	−0.0121	−0.0117	–
$\beta = 0°$	$\beta_r = 0°$	−0.012	−0.014	−0.007	−0.0053	−0.0042	−0.0060
$\beta = 0°$	$\beta_r = -+5°$	0.119	0.132	–	0.0009	0.0045	–
$\beta = 0°$	$\beta_r = +10°$	0.196	0.207	0.205	0.0049	0.0080	0.0061
$\beta = 0°$	$\beta_r = +20°$	0.370	0.393	0.397	0.0155	0.0179	0.0167
$\beta = 0°$	$\beta_r = +30°$	0.435	0.453	0.445	0.0212	0.0244	0.0201
$\beta = +10°$	$\beta_r = -20°$	2.220	2.558	2.519	−1.3331	−1.3699	−1.4337
$\beta = +10°$	$\beta_r = -10°$	2.459	2.801	2.753	−1.3227	−1.3586	−1.4216
$\beta = +10°$	$\beta_r = 0°$	2.705	3.059	2.993	−1.3064	−1.3403	−1.4060
$\beta = +10°$	$\beta_r = +10°$	3.017	3.406	3.307	−1.2842	−1.3173	−1.3850
$\beta = +10°$	$\beta_r = +20°$	3.140	3.505	3.423	−1.2798	−1.3131	−1.3816
$\beta = -10°$	$\beta_r = -20°$	−3.159	−3.485	−3.454	1.3024	1.3379	1.3975
$\beta = -10°$	$\beta_r = -10°$	−3.061	−3.402	−3.338	1.3054	1.3378	1.4007
$\beta = -10°$	$\beta_r = 0°$	−2.746	−3.073	−3.025	1.3270	1.3620	1.4214
$\beta = -10°$	$\beta_r = +10°$	−2.490	−2.815	−2.774	1.3439	1.3754	1.4365
$\beta = -10°$	$\beta_r = +20°$	−2.259	−2.576	−2.554	1.3564	1.3906	1.4502
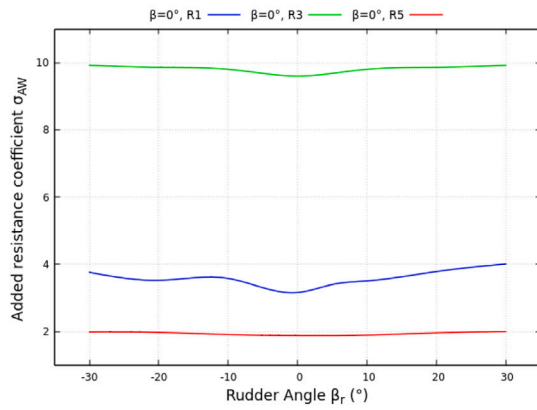
(a) Effect of rudder on σ_{AW} of zero-drift KCS in waves   (b) Effect of drift and rudder on σ_{AW} of KCS in waves
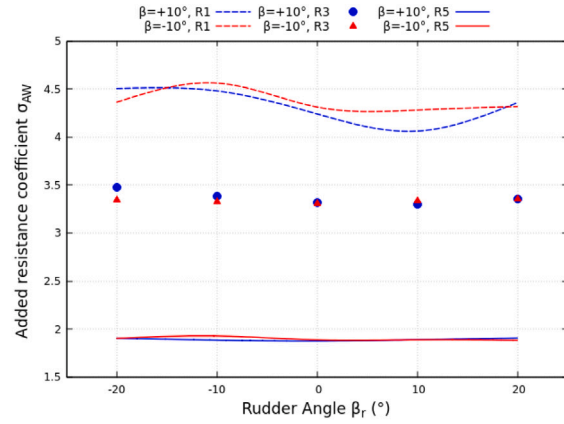
Fig. 13. Influence of drift and rudder angle on added resistance coefficient σ_{AW} of KCS in different wave conditions.

non-zero drift angles lead to the opposite shift: an ascending displacement of M_Z' curve is observed with a negative drift angle, whereas a positive drift angle leads to a descending trend. In addition, the presence of waves tends to alter the magnitude of the yaw moment coefficient slightly, and the yaw moment increases with the increment of wavelength, which is different from the wavelength influence on the ship's transverse force.

- Added resistance in waves

As shown in Fig. 6, the added resistance in waves can be obtained by:

$$R_T - R_{CW} = R_{AW} \quad (16)$$

Where R_T is the ship total resistance in waves, R_{CW} is the calm water resistance. R_{AW} is the added resistance in waves. A non dimensional added resistance coefficient σ_{AW} can be expressed as:

$$\sigma_{AW} = \frac{R_{AW} L_{PP}}{\rho g \zeta_0^2 B^2} \quad (17)$$

Where ζ_0 is the wave amplitude and B is the ship breadth, ρ is the density of water, and g is the gravity acceleration, L_{PP} is the ship length between perpendiculars.

The influence of static rudder angles and wavelength on the non-dimensional added resistance coefficient σ_{AW} of zero drift KCS in three

head waves is presented in Fig. 13(a). In terms of wave effect, it is found that medium wavelength R3 ($\lambda/L_{PP} = 1.15$) induces the highest added resistance while R5 wave ($\lambda/L_{PP} = 1.951$) generates the lowest σ_{AW} value. In addition, the effect of the rudder angle on the added resistance is significant, particularly in short wave cases R1. For example, when the rudder angle varies from 0° to +30°, the value of σ_{AW} is increased by approximately 27.1% in R1, while around 6.9% in R3 and 6.3% in R5. The overall trend is similar for all wave conditions: the applied non-zero rudder angles lead to higher wave-added resistance and the increment depends on the absolute magnitude of the rudder angle.

Fig. 13(b) illustrates the effect of drift on added resistance with varying rudder angles in short, medium, and long wave cases. Compared to medium and long waves, more noticeable variation can be found in short wave conditions: the peak of σ_{AW} occurs at $\beta_r = -10°$ when the drift angle is −10°, while the maximum value is at $\beta_r = -20°$ for $\beta = +10°$. In contrast to straight-ahead conditions, the influence of wavelength on σ_{AW} does not follow the same trend when the non-zero drift angle is applied: the shorter wavelength tends to induce a higher added resistance coefficient, therefore the highest σ_{AW} can be observed in short wave R1 cases ($\lambda/L_{PP} = 0.651$) for both drift scenarios while it happens in medium wave conditions at $\beta = 0°$.

Fig. 14 presents different model scales of KCS's added resistance coefficient σ_{AW} at straight-ahead conditions from both experimental and numerical results. Experimental results of FORCE, IIHR, and OU
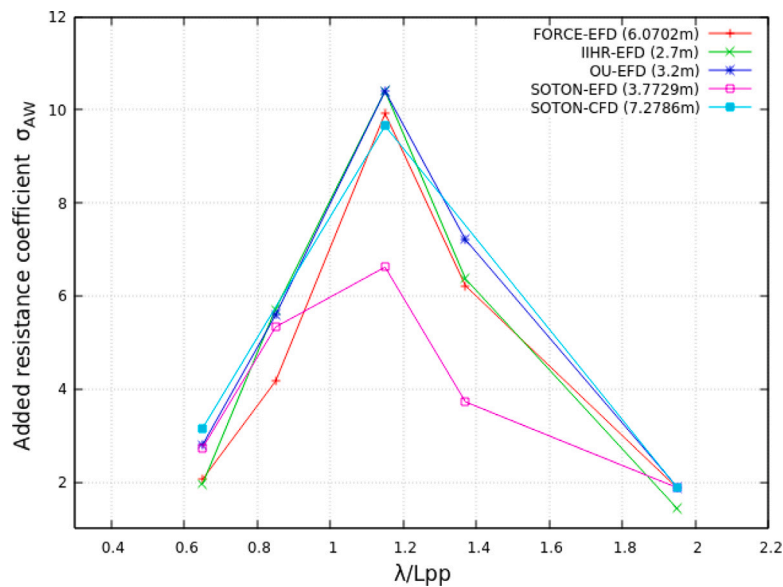
Fig. 14. Comparison between CFD and EFD data for zero drift KCS added resistance coefficient σ_{AW}.

are derived from Hino et al. (2020). Overall good consistency is found among all computed results, the maximum σ_{AW} happens at $\lambda/L_{PP} = 1.15$, which is around the resonance case. Compared to experimental findings from other academic institutions and the computational outcomes from SOTON, there is an evident discrepancy of SOTON experimental data at $\lambda/L_{PP} = 1.15$ and 1.37, which indicates further repeated tests should be conducted to eliminate experimental uncertainty. However, the numerical analyses from SOTON demonstrate a very good agreement with the experimental datasets presented at the 2015 Tokyo CFD workshop (Hino et al., 2020).

5.1.2. Influence of drift on rudder forces in waves

The influence of drift angle on rudder forces performance in medium wave R3 is shown in Fig. 15. Overall rudder forces variation follows the same trend as those in calm water. The presence of head waves leads to the increase of both rudder drag and lift. In terms of drag force, the value of C_D at the largest rudder angle magnitude scenario in R3 is increased by approximately 10.7%, 13%, and 4.5% than calm water condition in drift angle of 0°, +10° and −10°, indicating the combination effect of medium wave and positive drift is the most dominant among them. Similarly, the applied drift angle results in the vertical shift of the rudder lift C_L curve and the slope of the curve is steeper in medium wave R3 than that in calm water. To determine the effect of different wavelengths on rudder forces, rudder drag and lift coefficients in all considered cases are listed in Table 11. It is found that the medium wave R3 condition tends to induce the highest of both C_D and C_L values at most rudder angles for all drift cases though differences between three wave scenarios are quite tiny.

5.2. Hull–propeller–rudder interaction in waves

The time history of the hull, propeller, and rudder forces in short wave R1 is presented in Fig. 16, in which rpm = 900 is in period of 25 s to 50 s, rpm = 1200 is in period of 50 s to 75 s and rpm = 1500 is in period of 75 s to 100 s. Due to the presence of wave, all the forces oscillate with a certain degree of amplitude but have converged within 5 seconds' simulation time, which corresponds to 75, 100, and 125 propeller revolutions when rpm varying from 900, 1200, to 1500. To ensure to obtain a fully converged solution, the simulation is extended to run for 25 s for each rpm value. Compared to forces of the hull and propeller, rudder forces at the high propeller loading, mainly rudder lift, experience more significant oscillation, as shown in Fig. 16(c).

There are two main possible reasons: (1) High propeller loading induces higher velocity and more swirling flow into the rudder, which can cause irregular pressure distribution and unsteady forces on the rudder; (2) At high thrust loading, the wakefield becomes more asymmetric because of uneven thrust distribution, leading to unsteady forces and oscillation of rudder forces. The studies conducted by Simonsen and Stern (2005), Phillips et al. (2009), and Badoe et al. (2015) emphasize the difficulties in accurately predicting rudder forces, as they involve significant uncertainties and discrepancies between EFD and CFD results. These issues can be mitigated by adopting considerably finer mesh resolutions. Moreover, Date and Turnock (2002) suggests that approximately 5 to 20 million cells are necessary for the complete resolution of rudder forces. By weighing the trade-off between the required calculation accuracy and computational expenses, the mesh resolution implemented in this study can yield relatively accurate predictions of forces associated with ship manoeuvring in wave conditions.

5.2.1. Influence of drift on hull forces in waves

The effect of drift angle on KCS total resistance coefficients C_T in head waves is presented in Fig. 17(a). It is found that the applied non-zero drift angle leads to increases in drag force: the highest C_T occurs at negative rudder angles when a negative drift angle is applied while the maximum happens at positive rudder angles at $\beta = +10°$, although the trend of C_T increasing with rudder angle increments is the same for both drift KCS. However, when the negative static drift is applied, the effect of the rudder angle on drag is more apparent than in positive drift cases. The presence of an operating propeller does not change the influence of wavelength on total drag force: a higher wavelength still induces a higher value of C_T. Fig. 17(b) illustrates the effective drift angle influence on the net change of drag forces, benchmarking with zero drift scenarios. Although the applied drift angle results in increments of resistance coefficients in all considered cases: the net change of C_T increases with the ascending of the rudder angle from −20° to +20° for $\beta = +10°$ while the dC_T decreases with the same variation of the rudder angle for $\beta = −10°$. In addition, different wavelengths also affect the slope of the dC_T curve: for instance, in negative drift cases, the effect of long wave R5 is dominant in the negative rudder angle range while short wave R1 gives the steepest slope. Table 12 lists all values of total resistance coefficients in all considered cases and the resistance augments of dC_T benchmarking with calm water scenarios.
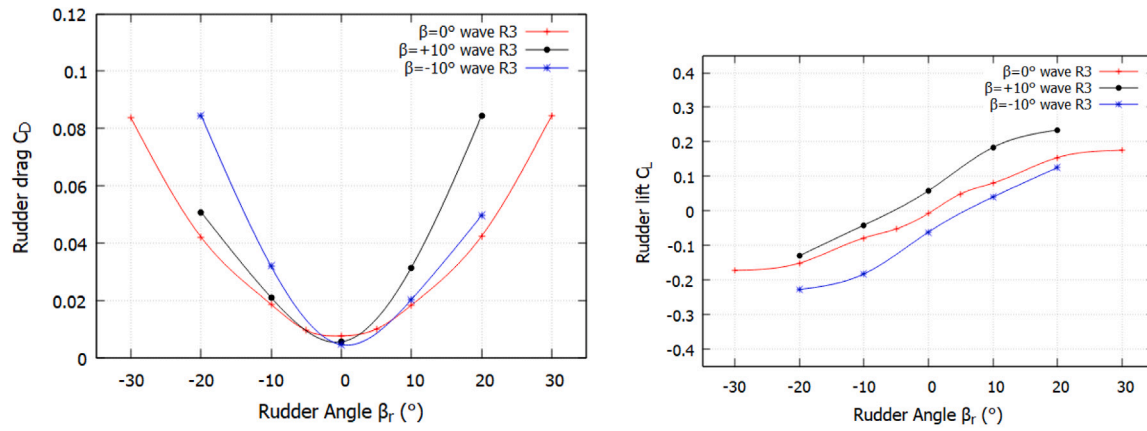
(a) Effect of drift on rudder drag performance in medium wave R3   (b) Effect of drift on rudder lift curve in medium wave R3

Fig. 15. Influence of drift and rudder angle on rudder forces in medium wave R3 conditions.

Table 11
Rudder drag (C_D) and lift coefficients (C_L) encountered by the KCS rudder in head waves.

Drift angle	Rudder angle	C_D			C_L		
		R1	R3	R5	R1	R3	R5
$\beta = 0°$	$\beta_r = -30°$	0.0785	0.0837	0.0831	−0.1648	−0.1719	−0.1711
$\beta = 0°$	$\beta_r = -20°$	0.0386	0.0421	0.0420	−0.1397	−0.1511	−0.1536
$\beta = 0°$	$\beta_r = -10°$	0.0174	0.0187	0.0173	−0.0725	−0.0782	−0.0766
$\beta = 0°$	$\beta_r = -5°$	0.0090	0.0096	–	−0.0496	−0.0521	–
$\beta = 0°$	$\beta_r = 0°$	0.0072	0.0077	0.0066	−0.0071	−0.0071	−0.0050
$\beta = 0°$	$\beta_r = +5°$	0.0093	0.0101	–	0.0449	0.0495	–
$\beta = 0°$	$\beta_r = +10°$	0.0172	0.0184	0.0171	0.0751	0.0805	0.0776
$\beta = 0°$	$\beta_r = +20°$	0.0395	0.0424	0.0419	0.1434	0.1544	0.1545
$\beta = 0°$	$\beta_r = +30°$	0.0794	0.0845	0.0838	0.1675	0.1755	0.1728
$\beta = +10°$	$\beta_r = -20°$	0.0492	0.0508	0.0478	−0.1247	−0.1299	−0.1216
$\beta = +10°$	$\beta_r = -10°$	0.0202	0.0210	0.0194	−0.0358	−0.0411	−0.0361
$\beta = +10°$	$\beta_r = 0°$	0.0052	0.0056	0.0052	0.0606	0.0584	0.0566
$\beta = +10°$	$\beta_r = +10°$	0.0319	0.0315	0.0335	0.1746	0.1839	0.1741
$\beta = +10°$	$\beta_r = +20°$	0.0844	0.0843	0.0861	0.2314	0.2342	0.2300
$\beta = -10°$	$\beta_r = -20°$	0.0848	0.0846	0.0855	−0.2264	−0.2271	−0.2271
$\beta = -10°$	$\beta_r = -10°$	0.0319	0.0319	0.0339	−0.1836	−0.1824	−0.1797
$\beta = -10°$	$\beta_r = 0°$	0.0044	0.0046	0.0045	−0.0636	−0.0613	−0.0598
$\beta = -10°$	$\beta_r = +10°$	0.0196	0.0203	0.0193	0.0344	0.0403	0.0364
$\beta = -10°$	$\beta_r = +20°$	0.0485	0.0496	0.0478	0.1221	0.1256	0.1207

In addition to the drag forces, the effect of static drift and rudder angles on KCS lateral force and yaw moment is shown in Table 13. Regarding side force encountered by KCS, a non-zero drift angle leads to the vertical shift: upwards for positive drift while downwards for negative drift, the same as the variation trend in calm water scenarios. The presence of waves tends to increase the displacement of the shift, and longer wavelength induces more significant displacement. However, the overall F_Y' curve slope does not change significantly with variations in drift angle and wavelength. When the propeller revolution rates rpm vary from 900 to 1200, the slope of the side force curve in three wave conditions also increases, but the change is very tiny. When the rpm further increases to 1500, the slope exhibits descending trend compared with the 1200rpm case. In terms of the yaw moment on KCS, the influence of drift angle, wavelength and propeller revolution rates on it is similar to side force, but the main difference is positive and negative drift angles lead to downward and upwards shifts, respectively. Compared to the longitudinal forces, it is concluded that the influence of static drift and rudder angle on KCS's transverse forces and yaw moment is less obvious, but it should be bear in mind that these two factors play crucial roles in ship manoeuvring in waves, particularly ship course keeping and turning abilities.

5.2.2. Drift influence on propeller performance in waves

The presence of the operating propeller accelerates the flow from the upstream hull to the downstream rudder, altering the flow distribution around the rudder. Likewise, when a rudder is positioned behind the propeller, it alters the flow conditions into the propeller plane, changing the actual thrust and torque the propeller induces. The influence of drift angle and rudder angle on the net change of the propeller thrust and torque, dK_T and $d10K_Q$ in regular waves at 900rpm is investigated by comparing the differences in drift and straight-ahead cases, as shown in Fig. 18.

In terms of propeller thrust augments, the applied drift angle gives rise to the reduction of the thrust coefficient in all considered cases. When the +10° drift angle is applied, the value of dK_T increases with the rudder angle varying from −20° to +20° in three wave conditions. In addition, the wavelength also affects the thrust augment curve: the shorter wavelength tends to have a more negative effect on propeller thrust. In contrast, the negative drift angle leads to the constant descending trend of the dK_T curve when the rudder angle changes from −20° to +20°, which indicates the applied negative drift angle has more disadvantageous impacts on propeller thrust coefficients than positive drift conditions. The wavelength effect on the dK_T curve in negative drifting is the same as in positive drift scenarios.
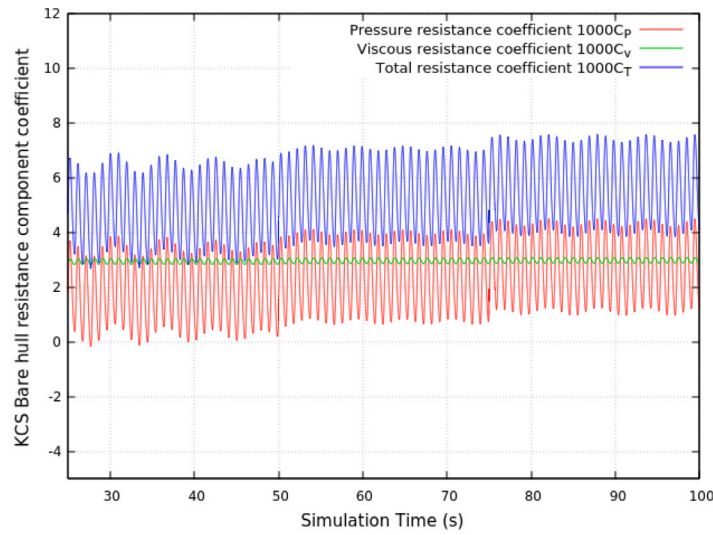
(a) Time history of KCS hull drag forces
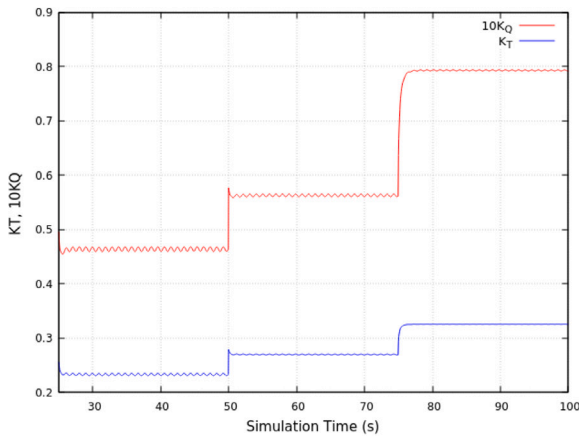
(b) Time history of propeller forces
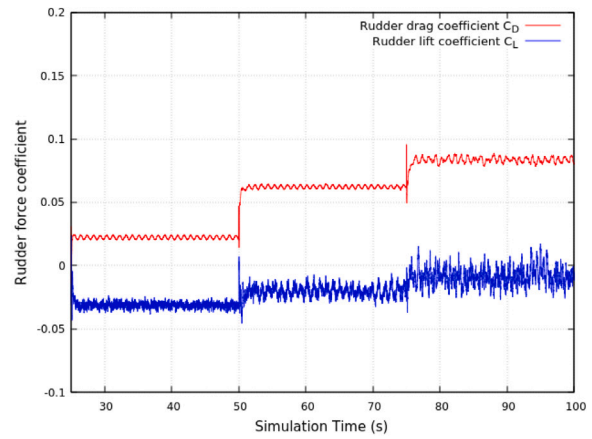
(c) Time history of rudder forces

Fig. 16. Time history of KCS hull, propeller and rudder forces in short wave R1 with rpm varying from 900, 1200 to 1500, $\beta = 0°$ and $\beta_r = 0°$.
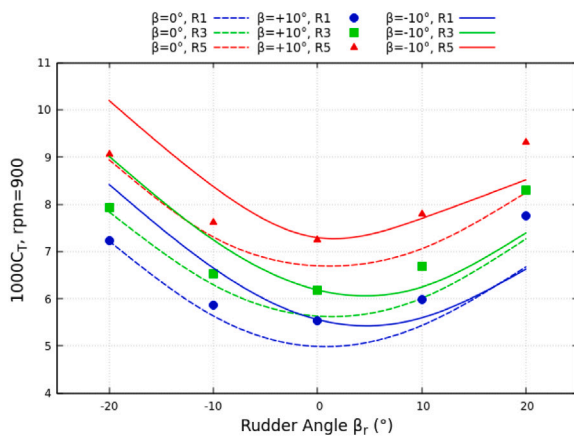
(a) Influence of drift on KCS C_T in three waves, rpm =900
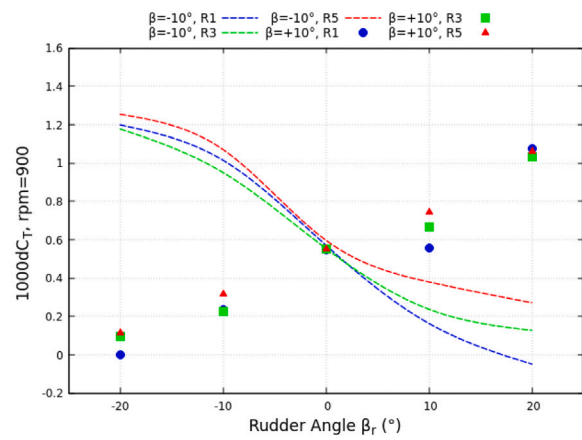
(b) Influence of drift on KCS dC_T in three waves, rpm =900

Fig. 17. Influence of drift on KCS resistance and resistance augment in three waves, rpm = 900, benchmarking with zero drift cases.

The static drift and rudder angle effect on the propeller torque augment is demonstrated in Fig. 18(b). In contrast to thrust, the drift effect on torque is more apparent. When the positive drift angle $\beta = +10°$ is employed and the rudder angle varies from $-20°$ to $+20°$,

the d10K_Q curve exhibits an increasing trend except for the rudder changing from $0°$ to $+10°$. Besides, the effect of the rudder angle on d10K_Q is almost consistent in three wave conditions: the ratio of d10K_Q values at $\beta_r = -20°$ and $\beta_r = +20°$ is approximately 1.98,

Table 12
Total ship resistance coefficients $1000C_T$ in three waves and augments $1000dC_T$ benchmarking with calm water scenarios.

		$\beta = 0°$	$\beta = +10°$	$\beta = -10°$	$\beta = 0°$	$\beta = +10°$	$\beta = -10°$
Short wave R1	β_r (°)	$1000C_T$	$1000C_T$	$1000C_T$	$1000dC_T$	$1000dC_T$	$1000dC_T$
rpm = 900	−20	7.220	7.222	8.419	0.334	0.306	0.276
	−10	5.637	5.871	6.651	0.407	0.271	0.235
	0	4.989	5.536	5.560	0.293	0.259	0.147
	10	5.432	5.989	5.595	0.414	0.240	0.229
	20	6.672	7.748	6.624	0.393	0.280	0.310
rpm = 1200	−20	8.803	8.800	9.935	0.385	0.283	0.233
	−10	7.086	7.145	7.788	0.422	0.243	0.182
	0	5.961	6.449	6.530	0.254	0.225	0.175
	10	6.463	7.323	6.546	0.312	0.245	0.113
	20	7.780	8.963	7.715	0.343	0.259	0.196
rpm = 1500	−20	9.322	9.432	10.204	0.429	0.190	0.273
	−10	7.701	7.965	8.280	0.433	0.235	0.233
	0	6.613	7.243	7.101	0.238	0.228	0.121
	10	7.002	7.847	7.103	0.327	0.167	0.053
	20	8.109	9.343	8.182	0.245	0.193	0.217
Medium wave R3							
rpm = 900	−20	7.838	7.936	9.015	0.951	1.020	0.872
	−10	6.297	6.524	7.247	1.068	0.924	0.832
	0	5.632	6.186	6.186	0.936	0.909	0.773
	10	6.009	6.677	6.247	0.991	0.928	0.880
	20	7.264	8.295	7.392	0.985	0.827	1.078
rpm = 1200	−20	9.472	9.535	10.560	1.054	1.017	0.858
	−10	7.722	7.823	8.438	1.059	0.921	0.832
	0	6.641	7.106	7.205	0.934	0.882	0.849
	10	7.096	7.971	7.231	0.945	0.892	0.798
	20	8.409	9.568	8.456	0.972	0.864	0.937
rpm = 1500	−20	9.963	10.167	10.861	1.070	0.925	0.930
	−10	8.323	8.662	8.942	1.054	0.932	0.895
	0	7.274	7.908	7.756	0.898	0.893	0.776
	10	7.647	8.534	7.802	0.972	0.854	0.752
	20	8.759	9.931	8.919	0.895	0.780	0.954
Long wave R5							
rpm = 900	−20	8.942	9.057	10.196	2.056	2.141	2.053
	−10	7.308	7.627	8.378	2.079	2.027	1.963
	0	6.698	7.251	7.294	2.001	1.973	1.881
	10	7.057	7.802	7.700	2.039	2.053	2.330
	20	8.247	9.308	8.518	1.967	1.840	2.205
rpm = 1200	−20	10.416	10.370	11.666	1.998	1.853	1.963
	−10	8.557	8.712	9.474	1.893	1.811	1.868
	0	7.594	8.010	8.155	1.887	1.786	1.800
	10	8.014	8.782	8.425	1.863	1.704	1.992
	20	9.213	10.440	9.383	1.776	1.736	1.864

1.81 and 2.05 in R1, R3 and R5. However, when the negative 10° drift angle is applied, the $d10K_Q$ exhibits ascending trend when the rudder angle is negative while descending in the positive rudder angle range. The peak of $d10K_Q$ occurs at around −5° rudder angle. The influence of wavelength on the torque augments is the same as that on thrust augments. Therefore it is indicated that the presence of short wave R1 tends to diminish the performance of propeller forces most in the three considered wave scenarios.

The findings above suggest the possible optimal operation strategy for the ship operating at the angle of drift in regular waves. The values of propeller thrust, torque coefficients in all cases are listed in Tables 14. It can be concluded that the imposed drift angle adversely impacts propeller performance in head waves to varying extents, which depend on the actual sea states the ship operates in, such as the effective drift angle, geometric rudder angle, wave characteristics, and propeller loading conditions.

### 5.2.3. The drift effect on rudder forces in waves

Accurate assessment of rudder forces when a ship operates in waves is essential for comprehensively understanding ship manoeuvrability and course-keeping capabilities in real seaways. The ship operator has to continuously fine-tune the rudder angle to maintain optimal navigation and performance throughout the vessel's journey. Figs. 19(a) and

19(b) present the influence of different rudder angles on rudder force performance when the ship operates at two static drift angles: −10° and +10° with propeller revolution rate rpm 900, in three different regular wave conditions.

The varying rudder angles' effect on the rudder drag is studied by comparing the differences in the net drag dC_D of the rudder in two drift conditions ($\beta = +10°$ and −10°), benchmarking with straight-ahead cases ($\beta = 0°$). When the KCS is applied with a positive drift angle, the dC_D curve varies with the increasing trend when the rudder angle changes from −20° to +20°. The same tendency can be observed for different wavelength cases, although different wavelengths have a slight effect on the dC_D curve. However, when KCS sails with a negative angle of drift, the varying rudder angles have the opposite effect on rudder drag augments: dC_D shows a descending variation with the rudder angle increasing from −20° to +20°. The overall trend for both drift angles is the dC_D curve exhibits central symmetry at the origin point, and the wave effect on rudder drag augments is relatively minor. Likewise, the effect of drift angle on rudder lift augments in head waves is illustrated in Fig. 19(b). The positive and negative drift angles yield corresponding positive and negative values of dC_L, respectively, but the overall variation trend of the lift augment curve is the same for both drifts: dC_L increases when the rudder varying from −20° to 0°, then shows the slightly descending and ascending trends when β_r changes

Table 13

KCS side force and yaw moment coefficients $1000F_Y'$ and $1000M_Z'$ in all considered cases.

		$\beta=0°$	$\beta=+10°$	$\beta=-10°$	$\beta=0°$	$\beta=+10°$	$\beta=-10°$
Short wave R1	β_r (°)	$1000F_Y'$	$1000F_Y'$	$1000F_Y'$	$1000M_Z'$	$1000M_Z'$	$1000M_Z'$
rpm = 900	−20	−0.952	1.356	−3.858	−0.045	−1.046	0.943
	−10	−0.714	1.900	−3.327	−0.038	−1.010	0.971
	0	−0.077	2.654	−2.668	−0.009	−0.981	1.004
	10	0.816	3.477	−1.814	0.032	−0.936	1.049
	20	1.266	3.950	−1.182	0.056	−0.907	1.078
rpm = 1200	−20	−0.973	1.410	−3.860	−0.039	−1.028	0.940
	−10	−0.720	1.897	−3.326	−0.030	−1.010	0.974
	0	−0.043	2.686	−2.539	−0.005	−0.971	1.009
	10	0.920	3.525	−1.694	0.040	−0.929	1.051
	20	1.453	4.115	−1.100	0.065	−0.895	1.078
rpm = 1500	−20	−0.834	1.757	−3.556	−0.024	−0.986	0.964
	−10	−0.577	1.908	−3.137	−0.016	−0.992	0.986
	0	−0.008	2.609	−2.309	−0.001	−0.957	1.018
	10	0.913	3.347	−1.656	0.041	−0.935	1.049
	20	1.338	3.935	−1.070	0.060	−0.887	1.074
Medium wave R3							
rpm = 900	−20	−0.946	1.735	−4.230	−0.045	−1.106	0.998
	−10	−0.714	2.272	−3.738	−0.039	−1.081	1.025
	0	−0.073	3.016	−3.045	−0.009	−1.041	1.062
	10	0.813	3.842	−2.185	0.033	−0.998	1.107
	20	1.249	4.348	−1.616	0.056	−0.967	1.137
rpm = 1200	−20	−0.975	1.773	−4.220	−0.039	−1.091	1.000
	−10	−0.713	2.283	−3.699	−0.031	−1.070	1.032
	0	−0.040	3.059	−2.928	−0.005	−1.033	1.069
	10	0.916	3.885	−2.057	0.041	−0.991	1.112
	20	1.446	4.471	−1.490	0.066	−0.958	1.140
rpm = 1500	−20	−0.830	2.118	−3.940	−0.024	−1.050	1.025
	−10	−0.573	2.300	−3.520	−0.017	−1.052	1.044
	0	−0.009	2.979	−2.720	0.001	−1.018	1.078
	10	0.900	3.720	−2.026	0.041	−0.981	1.111
	20	1.335	4.288	−1.453	0.060	−0.952	1.137
Long wave R5							
rpm = 900	−20	−0.978	2.027	−4.538	−0.046	−1.222	1.119
	−10	−0.684	2.589	−4.104	−0.036	−1.193	1.143
	0	−0.103	3.332	−3.369	−0.011	−1.157	1.180
	10	0.793	4.157	−2.587	0.030	−1.112	1.211
	20	1.228	4.625	−2.018	0.052	−1.089	1.243
rpm = 1200	−20	−0.995	2.148	−4.620	−0.039	−1.203	1.116
	−10	−0.642	2.622	−4.077	−0.028	−1.185	1.150
	0	−0.098	3.330	−3.297	−0.006	−1.149	1.185
	10	0.890	4.176	−2.418	0.037	−1.109	1.223
	20	1.407	4.791	−1.852	0.061	−1.077	1.251
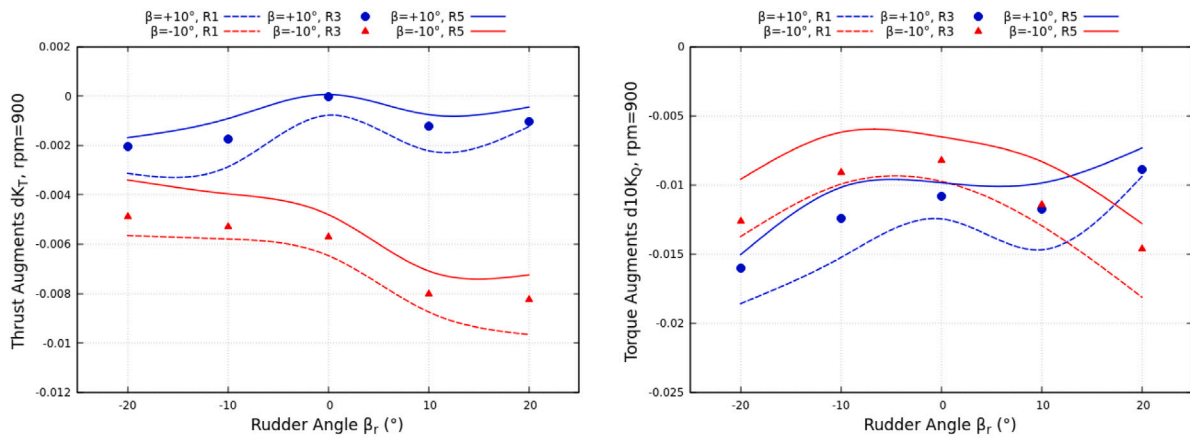
(a) Effect of drift angle on propeller thrust augments in waves   (b) Effect of drift angle on propeller torque augments waves

Fig. 18. Effect of drift angle on propeller forces in three waves, rpm = 900, benchmarking with zero drift cases.

Table 14

Propeller thrust and torque coefficients K_T and $10K_Q$ in all considered cases.

		$\beta = 0°$	$\beta = +10°$	$\beta = -10°$	$\beta = 0°$	$\beta = +10°$	$\beta = -10°$
Short wave R1	β_r (°)	K_T	K_T	K_T	$10K_Q$	$10K_Q$	$10K_Q$
rpm = 900	−20	0.2405	0.2374	0.2349	0.4834	0.4648	0.4696
	−10	0.2365	0.2336	0.2307	0.4708	0.4555	0.4608
	0	0.2331	0.2324	0.2267	0.4637	0.4512	0.4540
	10	0.2346	0.2324	0.2259	0.4665	0.4518	0.4535
	20	0.2377	0.2365	0.2281	0.4742	0.4648	0.4561
rpm = 1200	−20	0.2736	0.2684	0.2718	0.5754	0.5650	0.5707
	−10	0.2719	0.2663	0.2692	0.5675	0.5566	0.5625
	0	0.2699	0.2651	0.2674	0.5627	0.5524	0.5565
	10	0.2704	0.2660	0.2669	0.5643	0.5556	0.5552
	20	0.2713	0.2665	0.2677	0.5683	0.5560	0.5564
rpm = 1500	−20	0.3267	0.3217	0.3298	0.8032	0.7779	0.8468
	−10	0.3263	0.3213	0.3294	0.7984	0.7753	0.8419
	0	0.3255	0.3202	0.3291	0.7927	0.7686	0.8385
	10	0.3253	0.3201	0.3289	0.7913	0.7699	0.8361
	20	0.3253	0.3201	0.3288	0.7926	0.7702	0.8355
Medium wave R3							
rpm = 900	−20	0.2390	0.2370	0.2341	0.4794	0.4634	0.4668
	−10	0.2348	0.2331	0.2295	0.4665	0.4541	0.4574
	0	0.2316	0.2316	0.2259	0.4601	0.4493	0.4519
	10	0.2331	0.2319	0.2251	0.4626	0.4508	0.4512
	20	0.2363	0.2353	0.2281	0.4707	0.4618	0.4561
rpm = 1200	−20	0.2729	0.2681	0.2713	0.5734	0.5637	0.5690
	−10	0.2712	0.2662	0.2690	0.5656	0.5555	0.5615
	0	0.2693	0.2645	0.2670	0.5608	0.5503	0.5552
	10	0.2697	0.2655	0.2665	0.5624	0.5537	0.5534
	20	0.2706	0.2661	0.2676	0.5666	0.5551	0.5552
rpm = 1500	−20	0.3265	0.3220	0.3297	0.8017	0.7787	0.8455
	−10	0.3261	0.3216	0.3294	0.7967	0.7756	0.8406
	0	0.3253	0.3206	0.3290	0.7911	0.7695	0.8373
	10	0.3251	0.3205	0.3289	0.7899	0.7709	0.8353
	20	0.3251	0.3204	0.3288	0.7910	0.7701	0.8356
Long wave R5							
rpm = 900	−20	0.2384	0.2367	0.2350	0.4779	0.4628	0.4683
	−10	0.2339	0.2330	0.2299	0.4637	0.4535	0.4575
	0	0.2311	0.2311	0.2263	0.4580	0.4481	0.4514
	10	0.2326	0.2318	0.2255	0.4608	0.4509	0.4525
	20	0.2358	0.2354	0.2286	0.4691	0.4618	0.4563
rpm = 1200	−20	0.2724	0.2683	0.2713	0.5719	0.5623	0.5692
	−10	0.2707	0.2662	0.2691	0.5637	0.5542	0.5616
	0	0.2688	0.2646	0.2669	0.5587	0.5493	0.5546
	10	0.2693	0.2654	0.2665	0.5608	0.5515	0.5534
	20	0.2704	0.2664	0.2675	0.5656	0.5550	0.5548

from 0° to +20°. In addition, the presence of shorter wavelengths leads to higher absolute values of dC_L, although dC_L differences in the three waves are not significant.

All values of rudder forces, C_D and C_L are listed in Tables 15. These values offer an initial estimation of rudder force performance when a ship operates with a drift angle in waves, potentially contributing to more accurate approaches for assessing ship manoeuvring rudder performance in real sea states.

5.2.4. Influence of drift on the hull–propeller–wake interaction in waves

Thrust deduction and wake fraction are two critical parameters in assessing a vessel's propulsion efficiency and overall powering performance, they are defined in Eq. (18), in which R_{tow} is the resistance during the resistance test (without propeller) in waves, R_{prop} is the resistance during the fixed RPM test in waves, n is the rotation rate, the equivalent behind-hull advance ration J_i is derived from the open water results. The hull efficiency η_H is defined as the ratio of $1 - t$ and $1 - \omega_t$. Deriving the optimal hull efficiency requires the knowledge of how to maximize $(1 - t)$ and minimize $(1 - \omega_t)$. The influence of drift angle on the net change of $(1 - t)$ and $(1 - \omega_t)$ in waves, benchmarking with straight-ahead KCS, is presented in Figs. 20(a) and 20(b). For +10° drift cases, the $(1 - t)$ augments decrease with the varying rudder angle from −20° to +20° while this trend is opposite when −10°'drift

angle is applied. Regarding wave influence on the d$(1 - t)$ curve, short wave R1 results in the largest values of d$(1 - t)$ at all rudder angles for both +10° and −10° drift angles, while medium wave R3 leads to the smallest values of $(1 - t)$ augments. In terms of the drift influence on $(1 - \omega_t)$ augments shown in Fig. 20(b), +10° and −10° drift angle lead to decreasing and increasing trend with the rudder variation from −20° to +20°. Regarding the wavelength effect on d$(1 - \omega_t)$, the shortest wave R1 generates the highest $(1 - \omega_t)$ augment, and the longest wave R5 induces the lowest value. The values of $(1 - t)$, $(1 - \omega_t)$ in all considered cases are listed in Table 16.

$$1 - t = \frac{T + R_{tow} - R_{prop}}{T} \qquad 1 - \omega_t = \frac{V_{prop}}{V_{ship}} = \frac{J_i D_p n}{V_{ship}} \qquad (18)$$

The influences of different waves and propeller revolution rates on the hull efficiency η_H for three applied drift angles (0°, +10° and −10°) are presented in Fig. 21. For 0° and +10° drift cases, it is found that the optimal hull efficiency occurs at around zero rudder angle while the peak of η_H is located around +5° rudder angle for −10° drift cases, which is consistent with the calm water findings. In terms of the propeller revolution rates effect on η_H, the maximum hull efficiency can be found at rpm = 900 while the minimum is at rpm = 1200. In addition, different wavelengths also impact the distribution of hull efficiency: in all considered cases, the hull efficiency is the best in
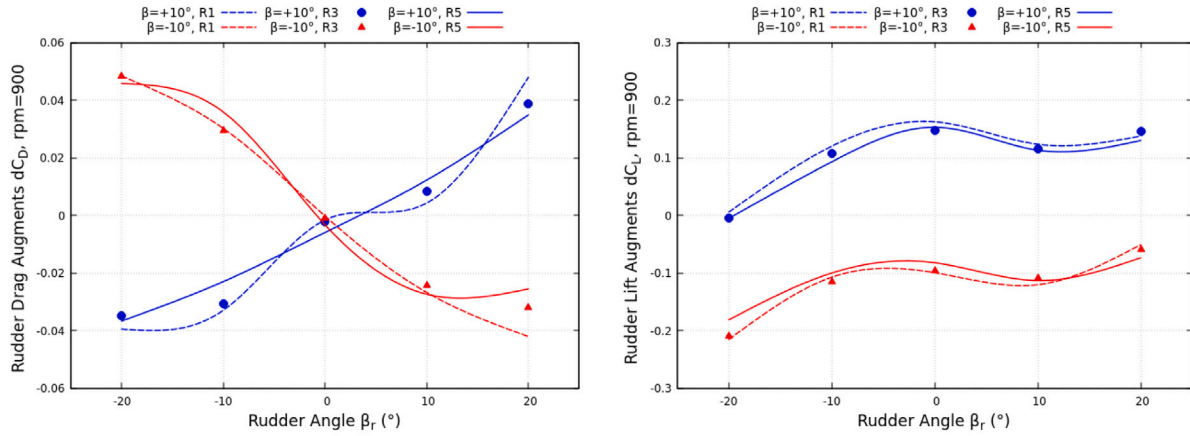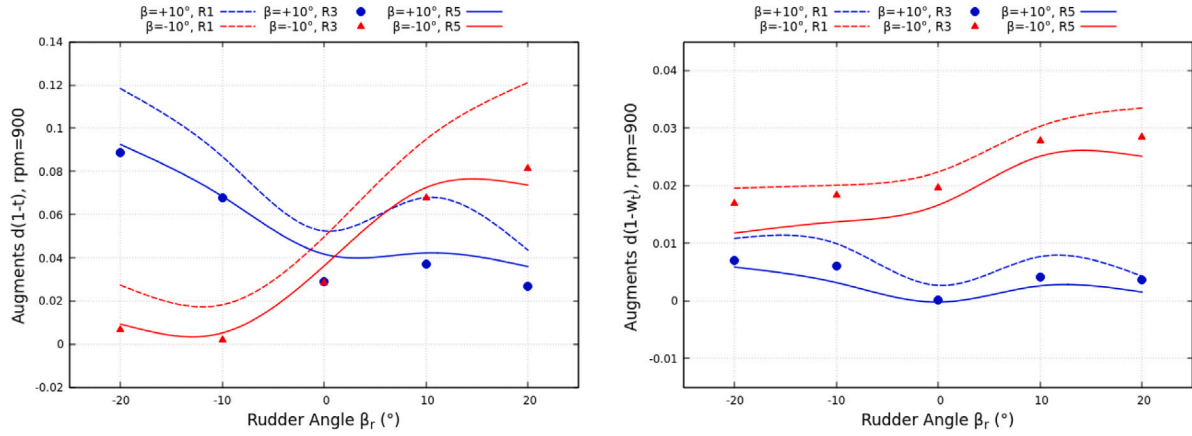
(a) Effect of drift angle on rudder drag augments in waves

(b) Effect of drift angle on rudder lift augments in waves

Fig. 19. Effect of drift angle on rudder forces in three waves, rpm = 900, benchmarking with zero drift cases.

Table 15
Rudder drag and lift coefficients C_D and C_L in all considered cases.

		$\beta = 0°$	$\beta = +10°$	$\beta = -10°$	$\beta = 0°$	$\beta = +10°$	$\beta = -10°$
Short wave R1	β_r (°)	C_D	C_D	C_D	C_L	C_L	C_L
rpm = 900	−20	0.2191	0.1797	0.2675	−0.3892	−0.3835	−0.6044
	−10	0.0857	0.0527	0.1158	−0.2877	−0.1675	−0.3948
	0	0.0223	0.0207	0.0221	−0.0311	0.1314	−0.1305
	10	0.0528	0.0571	0.0261	0.3293	0.4528	0.2090
	20	0.1596	0.2075	0.1176	0.5089	0.6466	0.4580
rpm = 1200	−20	0.3106	0.2705	0.3617	−0.4061	−0.3755	−0.6045
	−10	0.1575	0.1185	0.1793	−0.2993	−0.1795	−0.3995
	0	0.0621	0.0535	0.0656	−0.0200	0.1399	−0.0793
	10	0.0970	0.1242	0.0658	0.3687	0.4729	0.2584
	20	0.2114	0.2546	0.1692	0.5845	0.7115	0.4944
rpm = 1500	−20	0.3262	0.2830	0.3580	−0.3588	−0.2601	−0.4930
	−10	0.1800	0.1503	0.1912	−0.2503	−0.1915	−0.3283
	0	0.0835	0.0830	0.0845	−0.0085	0.0952	0.0123
	10	0.1140	0.1310	0.0827	0.3657	0.3872	0.2761
	20	0.2105	0.2525	0.1790	0.5383	0.6246	0.5108
Medium wave R3							
rpm = 900	−20	0.2184	0.1837	0.2666	−0.3859	−0.3900	−0.5948
	−10	0.0850	0.0545	0.1146	−0.2866	−0.1797	−0.4013
	0	0.0229	0.0206	0.0220	−0.0294	0.1187	−0.1250
	10	0.0519	0.0604	0.0276	0.3274	0.4427	0.2188
	20	0.1599	0.1986	0.1279	0.5027	0.6483	0.4445
rpm = 1200	−20	0.3111	0.2749	0.3576	−0.4062	−0.3862	−0.5919
	−10	0.1577	0.1195	0.1788	−0.2953	−0.1847	−0.3909
	0	0.0636	0.0524	0.0660	−0.0201	0.1328	−0.0808
	10	0.0986	0.1217	0.0686	0.3665	0.4596	0.2691
	20	0.2130	0.2515	0.1751	0.5817	0.6980	0.4975
rpm = 1500	−20	0.3258	0.2878	0.3575	−0.3574	−0.2737	−0.4906
	−10	0.1794	0.1535	0.1925	−0.2476	−0.1948	−0.3243
	0	0.0845	0.0837	0.0835	−0.0109	0.0844	0.0030
	10	0.1140	0.1309	0.0868	0.3596	0.3766	0.2830
	20	0.2120	0.2494	0.1854	0.5372	0.6099	0.5156
Long wave R5							
rpm = 900	−20	0.2239	0.1873	0.2696	−0.3999	−0.4049	−0.5810
	−10	0.0814	0.0584	0.1173	−0.2761	−0.1831	−0.4165
	0	0.0251	0.0192	0.0219	−0.0418	0.1112	−0.1240
	10	0.0542	0.0665	0.0269	0.3210	0.4341	0.2080
	20	0.1587	0.1936	0.1332	0.4962	0.6262	0.4227
rpm = 1200	−20	0.3140	0.2683	0.3715	−0.4164	−0.3656	−0.6224
	−10	0.1502	0.1170	0.1832	−0.2660	−0.1788	−0.4087
	0	0.0661	0.0521	0.0668	−0.0446	0.1079	−0.0994
	10	0.0992	0.1149	0.0821	0.3580	0.4402	0.2592
	20	0.2076	0.2511	0.1772	0.5683	0.6924	0.4872

(a) Effect of drift angle on $1 - t$ augments in three waves

(b) Effect of drift angle on $1 - \omega_t$ augments in three waves

Fig. 20. Effect of drift angle on $1 - t$ and $1 - \omega_t$ augments in three waves, rpm = 900, benchmarking with zero drift cases.

Table 16
Thrust deduction and wake fraction $(1 - t)$ and $(1 - \omega_t)$ in all considered cases.

		$\beta = 0°$	$\beta = +10°$	$\beta = -10°$	$\beta = 0°$	$\beta = +10°$	$\beta = -10°$
Short wave R1	β_r (°)	$1 - t$	$1 - t$	$1 - t$	$1 - \omega_t$	$1 - \omega_t$	$1 - \omega_t$
rpm = 900	−20	0.671	0.789	0.698	1.010	1.021	1.030
	−10	0.820	0.907	0.838	1.024	1.034	1.044
	0	0.877	0.929	0.926	1.036	1.039	1.058
	10	0.842	0.910	0.936	1.031	1.038	1.061
	20	0.730	0.774	0.851	1.020	1.024	1.053
rpm = 1200	−20	0.752	0.808	0.771	1.194	1.219	1.203
	−10	0.833	0.884	0.860	1.202	1.228	1.215
	0	0.887	0.914	0.911	1.211	1.234	1.223
	10	0.866	0.882	0.917	1.209	1.229	1.225
	20	0.807	0.820	0.869	1.205	1.227	1.222
rpm = 1500	−20	0.852	0.879	0.871	1.187	1.215	1.168
	−10	0.893	0.914	0.913	1.189	1.217	1.170
	0	0.921	0.931	0.938	1.193	1.224	1.172
	10	0.913	0.922	0.941	1.195	1.224	1.173
	20	0.887	0.893	0.918	1.194	1.225	1.174
Medium wave R3							
rpm = 900	−20	0.706	0.795	0.713	1.016	1.023	1.033
	−10	0.849	0.916	0.851	1.030	1.036	1.048
	0	0.910	0.939	0.938	1.041	1.041	1.061
	10	0.879	0.916	0.947	1.036	1.040	1.064
	20	0.767	0.794	0.849	1.025	1.029	1.053
rpm = 1200	−20	0.767	0.810	0.777	1.197	1.220	1.205
	−10	0.849	0.887	0.863	1.205	1.229	1.216
	0	0.901	0.919	0.914	1.214	1.236	1.225
	10	0.882	0.887	0.920	1.212	1.232	1.227
	20	0.823	0.827	0.869	1.208	1.229	1.222
rpm = 1500	−20	0.861	0.880	0.874	1.187	1.213	1.169
	−10	0.902	0.915	0.914	1.190	1.216	1.171
	0	0.929	0.933	0.940	1.194	1.222	1.173
	10	0.921	0.923	0.942	1.196	1.222	1.174
	20	0.896	0.897	0.918	1.195	1.223	1.174
Long wave R5							
rpm = 900	−20	0.628	0.720	0.637	1.018	1.024	1.030
	−10	0.776	0.844	0.781	1.033	1.037	1.047
	0	0.830	0.872	0.867	1.043	1.043	1.060
	10	0.803	0.845	0.875	1.038	1.040	1.063
	20	0.700	0.736	0.774	1.027	1.028	1.052
rpm = 1500	−20	0.737	0.789	0.743	1.200	1.219	1.205
	−10	0.823	0.863	0.835	1.208	1.229	1.215
	0	0.869	0.895	0.889	1.217	1.236	1.225
	10	0.852	0.869	0.881	1.214	1.232	1.227
	20	0.800	0.806	0.844	1.209	1.228	1.222

medium wave R3 conditions, while the worst is found in long wave R5 scenarios.

6. Conclusions

In this paper, a comprehensive numerical study of drift angle combined with rudder angle effect on a fully appended container ship KCS model in regular wave conditions is presented. The unsteady Reynolds-averaged Navier–Stokes (URANS) solver coupled with Blade Element Momentum Theory (BEMt) is achieved using OpenFOAM to predict ship's manoeuvring and powering performance in waves.

According to the literature review presented in Section 1, traditional experimental approaches for evaluating ship manoeuvring performance are very costly and have high requirements for test facilities and ship models. In comparison, the numerical approach is a more cost-efficient alternative for determining the ship's manoeuvring performance in waves. However, full 6DOF dynamic manoeuvring models (CFD-based direct simulation methods) still remain computationally expensive due to the extensive computing resource needed for resolving interactions among ship motion, wakefield, the hydrodynamic forces acting on the vessel, rotating propeller and rudder. Furthermore, one key challenge related to these calculations is the process of validation. Guaranteeing the accuracy of these simulations requires dependable and accurate experimental data, the acquisition of which, unfortunately, is very difficult and costly. Thus, this study aims to enhance the understanding of ship manoeuvring in waves by simulating the fully appended KCS model with combined drift and rudder angles in head waves with varying propeller thrust loading conditions. This cost-effective numerical approach not only captures the quasi-static phases of a ship's manoeuvre in waves but also eliminates the need to model the entire transient manoeuvre, significantly cutting down computational efforts. By conducting simulations at fixed angles, we gain a precise understanding of the fluid dynamics around the ship's hull and rudder under controlled conditions. Crucially, this approach enables the development of Reduced Order Models (ROMs) by utilizing hydrodynamic coefficients derived from force measurements at various rudder and drift angles. These ROMs are essential for constructing a real-time ship manoeuvrability simulator. While full 6DOF simulations are impractical for real-time applications, using a finite set of angles allows us to collect adequate data to develop effective ROMs efficiently and cost-effectively. Compared to the direct simulation of ship manoeuvring, the simulation under static drift and rudder conditions allows for direct validation and contributes to the future validation process of the actual dynamic manoeuvring models and simulations in waves.

For all considered cases, resistance tests at the ship's design speed in three different regular head wave conditions are initially conducted, followed by three different fixed RPM tests. Numerical propeller modelling is accomplished using the Blade Element Momentum Theory (BEMt), which simplifies the KCS propeller geometry into basic distributions of pitch and chord, rather than utilizing the complete geometry. To verify the accuracy and reliability of the numerical results, the experimental results related to the Southampton scale KCS model drag were used to compare CFD results of three wavelengths. The principal findings of this study are outlined below:

- In terms of hull–rudder interaction in waves, longer wavelength results in an increasing trend of hull resistance for all drift scenarios but the applied non-zero drift angle tends to weaken this ascending trend. The largest hull side force occurs at medium wave for all drift cases while the hull yaw moment increases with the increment of wavelength. The rudder forces in regular head waves follows a similar trend as those in calm water (Zhang et al., 2023) but the presence of wave results in steeper slopes of both C_D and C_L curves. The highest added resistance coefficient is found in medium wave for straight ahead condition while it decreases with the wavelength increment when the non-zero drift angle is applied.
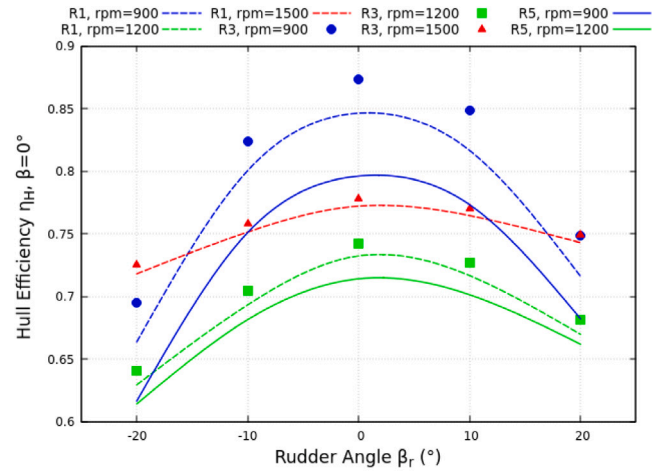
(a) Effect of rudder and propeller rpm on η_H in waves, $\beta = 0\,°$
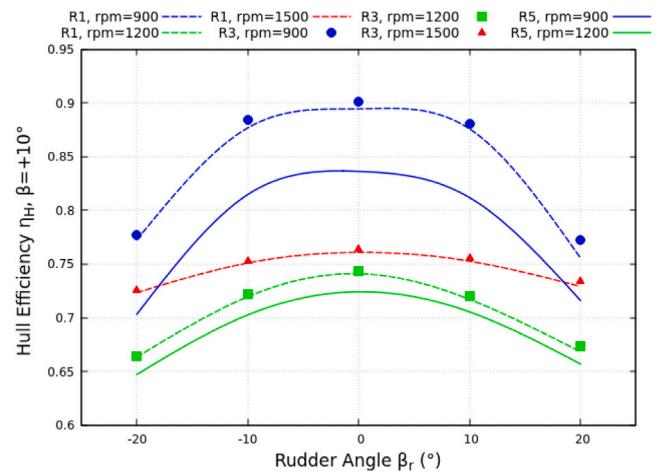
(b) Effect of rudder and propeller rpm on η_H in waves, $\beta = +10\,°$
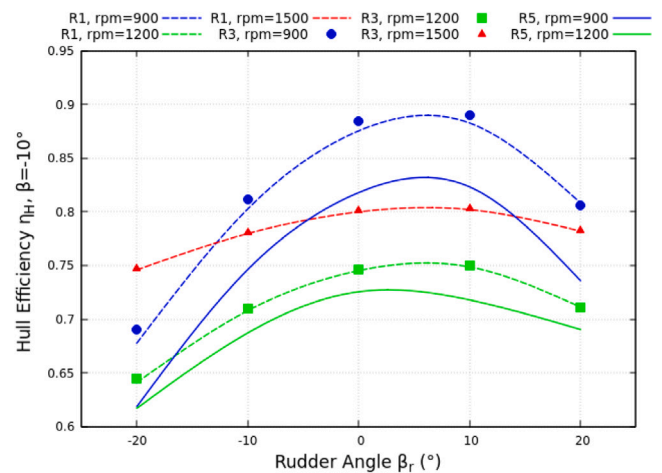
(c) Effect of rudder and propeller rpm on η_H in waves, $\beta = -10\,°$

Fig. 21. Effect of rudder angle and propeller revolution rate on hull efficiency η_H in waves.

- Experimental data of total resistance coefficient (C_T) obtained from the Southampton scale KCS model is compared with the CFD results at the straight ahead condition ($\beta = 0°$) for three head waves: overall good agreement is found between EFD and CFD but the usage of different types of rudder (all movable rudder in EFD while semi-balanced rudder in CFD) and different wave motions lead to some discrepancies, and this kind of deviation is more evident in medium and long wave conditions.
- For hull–propeller–rudder interaction in waves, longer wavelength and higher propeller loading conditions contributes to the increment of both total resistance coefficients (C_T) and net change of C_T (dC_T) compared to calm water cases. This increasing contribution is more obvious in straight ahead and positive drift cases than negative drift scenarios. Shorter wavelength has more negative impact on propeller performance in waves for non-zero drift cases. Different from calm water scenarios, the effect of drift angle on propeller performance in waves depends on wave properties and propeller loading conditions. Effect of drift on rudder forces in waves depends on the sign of both drift and rudder angles, wavelength has little impact on rudder force curves.
- The influence of drift angle on the hull efficiency in regular head waves follows the same pattern as calm water conditions: the applied drift angle can affect the rudder angle position at optimal hull efficiency, 0°rudder angle for zero and positive drift cases while around +5°rudder angle for negative drift scenarios. Under the same propeller loading conditions, medium wavelength R3 results in the highest hull efficiency while the lowest η_H is found in long wavelength R5.

In conclusion, this paper facilitates a deeper understanding of ship manoeuvring in waves by studying the influence of drift and rudder angles on the hull–propeller–rudder–wake interaction in regular head waves with varying propeller thrust loading conditions. This investigation makes it possible to provide some good insights into better ship design assessment due to ship manoeuvring in waves and operations of wind-assist vessels. For operating wind-assist vessels, the drift angle effect analysis allows for the successful integration of wind propulsion devices such as wing sails on conventional commercial vessels and it ensures that wind-assisted devices can generate thrust efficiently and help to maintain the desired course of vessels. Future research should focus on obtaining high-quality experimental data to ensure comprehensive validation and verification. Another is to carry out simulations of full-scale ships and also more realistic sea states such as irregular waves.

Data availability

Data will be made available on request.

CRediT authorship contribution statement

Yifu Zhang: Writing – review & editing, Writing – original draft, Visualization, Validation, Software, Methodology, Conceptualization. **Héctor Rubén Díaz-Ojeda:** Writing – review & editing, Software, Methodology, Investigation. **Björn Windén:** Writing – review & editing, Software, Methodology, Investigation, Conceptualization. **Dominic Hudson:** Writing – review & editing, Supervision, Investigation. **Stephen Turnock:** Writing – review & editing, Supervision, Methodology, Investigation, Conceptualization.

Declaration of competing interest

The authors declare that they have no known competing financial interests or personal relationships that could have appeared to influence the work reported in this paper.

References

Aung, M.Z., Umeda, N., 2020. Manoeuvring simulations in adverse weather conditions with the effects of propeller and rudder emergence taken into account. Ocean Eng. 197, 106857.

Badoe, C.E., Phillips, A.B., Turnock, S.R., 2015. Influence of drift angle on the computation of hull–propeller–rudder interaction. Ocean Eng. 103, 64–77.

Bowker, J., Buckland, D., Gregory, M., Townsend, N., Zhang, Y., Turnock, S., 2023. A free running instrumented container ship model for investigating energy efficiency in waves.

Burrill, L., 1944. Calculation of Marine Propeller Performance Characteristics. Volume 60, The North East Coast Institution of Engineers and Shipbuilders, Bolbec Hall, Newcastle upon Tyne, UK, Institution Transactions.

Carrica, P.M., Ismail, F., Hyman, M., Bhushan, S., Stern, F., 2013. Turn and zigzag maneuvers of a surface combatant using a URANS approach with dynamic overset grids. J. Mar. Sci. Technol. 18, 166–181.

Choi, H.j., Kim, D.j., Kim, Y.g., Yeo, D.j., Yoon, G.h., Lee, G.j., 2019. An experimental study on the captive model test of kcs in regular waves.

Date, J.C., Turnock, S.R., 2002. Computational evaluation of the periodic performance of a NACA 0012 fitted with a Gurney flap. J. Fluids Eng. 124 (1), 227–234.

Du, P., Cheng, L., Tang, Z.j., Ouahsine, A., Hu, H.b., Hoarau, Y., 2022. Ship maneuvering prediction based on virtual captive model test and system dynamics approaches. J. Hydrodyn. 34 (2), 259–276.

Ferziger, J.H., Perić, M., Street, R.L., 2019. Computational Methods for Fluid Dynamics. springer.

Gatin, I., Vukcevic, V., Jasak, H., Lalovic, I., 2018. Manoeuvring simulations using the overset grid technology in foam-extend. In: 32nd Symposium on Naval Hydrodynamics.

Hasnan, M., Yasukawa, H., Hirata, N., Terada, D., Matsuda, A., 2020. Study of ship turning in irregular waves. J. Mar. Sci. Technol. 25 (4), 1024–1043.

Hino, T., Stern, F., Larsson, L., Visonneau, M., Hirata, N., Kim, J., 2020. Numerical Ship Hydrodynamics: An Assessment of the Tokyo 2015 Workshop. vol. 94, Springer Nature.

Hirano, M., Takashina, J., Takaishi, Y., Saruta, T., 1980. Ship turning trajectory in regular waves. In: Publication of: West Japan Society of Naval Architects. (60).

Islam, H., Soares, C.G., 2018. Estimation of hydrodynamic derivatives of a container ship using pmm simulation in openfoam. Ocean Eng. 164, 414–425.

ITTC, 2014. Practical guidelines for ship CFD applications ITTC–recommended procedures and guidelines. In: International Towing Tank Conference Section. 7, pp. 03–02.

ITTC, 2017. Uncertainty analysis in CFD verification and validation methodology and procedures. In: ITTC-Recommended Procedures and Guidelines. pp. 1–13.

ITTC, 2021. The Specialist Committee on Manoeuvring in Waves - Final Report and Recommendations to the 29th ITTC. Technical Report..

Kim, D., Song, S., Tezdogan, T., 2021. Free running CFD simulations to investigate ship manoeuvrability in waves. Ocean Eng. 236, 109567.

Larsson, L., Stern, F., Visonneau, M., 2013. Numerical Ship Hydrodynamics: An Assessment of the Gothenburg 2010 Workshop. Springer.

Lee, J.H., Kim, Y., 2020. Study on steady flow approximation in turning simulation of ship in waves. Ocean Eng. 195, 106645.

Menter, F.R., 1994. Two-equation eddy-viscosity turbulence models for engineering applications. AIAA J. 32 (8), 1598–1605.

Menter, F.R., Kuntz, M., Langtry, R., et al., 2003. Ten years of industrial experience with the SST turbulence model. Turbul. Heat Mass Transf. 4 (1), 625–632.

MEPC, R., 2017. 2013 Interim guidelines for determing minimum propulsion power to maintain the manoeuvrability of ships in adverse conditions.

Molland, A.F., Turnock, S.R., Hudson, D.A., 2017. Ship Resistance and Propulsion. Cambridge University Press.

Nonaka, K., 1990. Manoeuvring motion of a ship in waves. In: Proc Joint Int Conf Marine Simulation and Ship Manoeuvrability.

OpenFOAM Foundation, 2023. Openfoam. https://openfoam.org/.

OpenFOAMFoundation, 2019. Openfoam version 7. URL: https://openfoam.org/download/7-source/.

Papanikolaou, A., Fournarakis, N., Chroni, D., Liu, S., Plessas, T., Sprenger, F., 2016. Simulation of the maneuvering behavior of ships in adverse weather conditions. In: Proceedings. pp. 11–16.

Paramesh, S., Rajendran, S., 2021. A unified seakeeping and manoeuvring model with a PID controller for path following of a KVLCC2 tanker in regular waves. Appl. Ocean Res. 116, 102860.

Phillips, A.B., Turnock, S.R., Furlong, M., 2009. Evaluation of manoeuvring coefficients of a self-propelled ship using a blade element momentum propeller model coupled to a Reynolds averaged Navier Stokes flow solver. Ocean Eng. 36 (15–16), 1217–1225.

Piro, D., White, P., Knight, B., Maki, K., Kring, D., 2020. Prediction of ship maneuvering in waves using a combined RANS and potential flow approach. In: Proceedings of 33rd Symposium on Naval Hydrodynamics.

Sanada, Y., Elshiekh, H., Toda, Y., Stern, F., 2019. ONR tumblehome course keeping and maneuvering in calm water and waves. J. Mar. Sci. Technol. 24, 948–967.

Sanada, Y., Tanimoto, K., Takagi, K., Gui, L., Toda, Y., Stern, F., 2013. Trajectories for ONR tumblehome maneuvering in calm water and waves. Ocean Eng. 72, 45–65.

Seo, M.G., Kim, Y., 2011. Numerical analysis on ship maneuvering coupled with ship motion in waves. Ocean Eng. 38 (17–18), 1934–1945.

Shen, Z., Korpus, R., 2015. Numerical simulations of ship self-propulsion and maneuvering using dynamic overset grids in openfoam. In: Proceedings of the Tokyo.

Shigunov, V., El Moctar, O., Papanikolaou, A., Potthoff, R., Liu, S., 2018. International benchmark study on numerical simulation methods for prediction of manoeuvrability of ships in waves. Ocean Eng. 165, 365–385.

SIMMAN, 2008. SIMMAN2008 worshop on verification and validation of ship manoeuvring simulation methods. URL: http://www.simman2008.dk/.

SIMMAN, 2014. SIMMAN2014 worshop on verification and validation of ship manoeuvring simulation methods. URL: http://www.simman2014.dk/.

SIMMAN, 2020. SIMMAN2020 worshop on verification and validation of ship manoeuvring simulation methods. URL: http://www.simman2020.kr/.

Simonsen, C.D., Otzen, J.F., Klimt, C., Larsen, N.L., Stern, F., 2012. Maneuvering predictions in the early design phase using CFD generated PMM data. In: 29th Symposium on Naval Hydrodynamics. pp. 26–31.

Simonsen, C.D., Stern, F., 2005. RANS maneuvering simulation of esso osaka with rudder and a body-force propeller. J. Ship Res. 49 (02), 98–120.

Skejic, R., Faltinsen, O.M., 2008. A unified seakeeping and maneuvering analysis of ships in regular waves. J. Mar. Sci. Technol. 13, 371–394.

Sprenger, F., Maron, A., Delefortrie, G., Van Zwijnsvoorde, T., Cura-Hochbaum, A., Lengwinat, A., Papanikolaou, A., 2017. Experimental studies on seakeeping and maneuverability of ships in adverse weather conditions. J. Ship Res. 61 (03), 131–152.

Stern, F., Agdraup, K., Kim, S., Hochbaum, A., Rhee, K., Quadvlieg, F., Perdon, P., Hino, T., Broglia, R., Gorski, J., 2011. Experience from SIMMAN 2008—the first workshop on verification and validation of ship maneuvering simulation methods. J. Ship Res. 55 (02), 135–147.

Stern, F., Wilson, R.V., Coleman, H.W., Paterson, E.G., 2001. Comprehensive approach to verification and validation of cfd simulations—part 1: methodology and procedures. J. Fluids Eng. 123 (4), 793–802.

Subramanian, R., Beck, R.F., 2015. A time-domain strip theory approach to maneuvering in a seaway. Ocean Eng. 104, 107–118.

Sung, Y.J., Park, S.H., 2015. Prediction of ship manoeuvring performance based on virtual captive model tests. J. Soc. Naval Archit. Korea 52 (5), 407–417.

Suzuki, R., Ueno, M., Tsukada, Y., 2021. Numerical simulation of 6-degrees-of-freedom motions for a manoeuvring ship in regular waves. Appl. Ocean Res. 113, 102732.

Tello Ruiz, M., Mansuy, M., Donatini, L., Villagomez, J., Delefortrie, G., Lataire, E., Vantorre, M., 2019. Wave effects on the turning ability of an ultra large container ship in shallow water. In: International Conference on Offshore Mechanics and Arctic Engineering. 58844, American Society of Mechanical Engineers, V07AT06A065.

Turnock, S., Hosseinzadeh, S., Zhang, Y., Bowker, J., Buckland, D., Gregory, M., Townsend, N., 2024. Hull-propeller-rudder interactions: time-accurate data of a scaled model ship in waves. Ocean Eng. 312, 119258.

Wang, J.-h., Wan, D.-c., 2016. Investigations of self-propulsion in waves of fully appended onr tumblehome model. Appl. Math. Mech. (1000-0887) 37 (12).

Wang, J., Wan, D., 2018. Direct simulations of turning circle maneuver in waves using RANS-overset method. In: International Conference on Offshore Mechanics and Arctic Engineering. 51333, American Society of Mechanical Engineers, V11BT12A013.

Wang, J., Zou, L., Wan, D., 2018. Numerical simulations of zigzag maneuver of free running ship in waves by RANS-overset grid method. Ocean Eng. 162, 55–79.

White, P., 2020. A Hybrid Computational Framework for the Simulation of Ships Maneuvering In Waves (Ph.D. thesis).

White, P.F., Piro, D.J., Knight, B.G., Maki, K.J., 2022. A hybrid numerical framework for simulation of ships maneuvering in waves. J. Ship Res. 66 (02), 159–171.

Windén, B., 2014. Powering performance of a self-propelled ship in waves (Ph.D. thesis). University of Southampton.

Windén, B., 2021a. An open-source framework for ship performance CFD. In: SNAME Offshore Symposium. SNAME, D021S003R002.

Windén, B., 2021b. Predicting the powering performance of different vessel types using an open-source CFD propulsion framework. In: SNAME Maritime Convention. SNAME, D021S004R004.

Yasukawa, H., 2006. Simulation of wave-induced motions of a turning ship. J. Japan Soc. Naval Archit. Ocean Eng. 4, 117–126.

Yasukawa, H., Amri Adnan, F., Nishi, K., 2010. Wave-induced motions on a laterally drifting ship. Ship Technol. Res. 57 (2), 84–98.

Yasukawa, H., Faizul, A.A., 2006. Experimental study on wave-induced motions and steady drift forces of an obliquely moving ship. J. Japan Soc. Naval Archit. Ocean Eng. 3, 133–138.

Yasukawa, H., Nakayama, Y., 2009. 6-DOF motion simulations of a turning ship in regular waves. In: Proceedings of the International Conference on Marine Simulation and Ship Manoeuvrability. pp. 508–517.

Yasukawa, H., Zaky, M., Yonemasu, I., Miyake, R., 2017. Effect of engine output on maneuverability of a VLCC in still water and adverse weather conditions. J. Mar. Sci. Technol. 22, 574–586.

Zhang, Y., 2023. Influence of drift angle on the self-propelled ship's powering performance in waves (Ph.D. thesis). University of Southampton.

Zhang, Y., Hosseinzadeh, S., Banks, J., Hudson, D., Turnock, S., 2023. Influence of Leeway on Hull-Propeller-Rudder Interaction Using CFD Methods. Norwegian University of Science and Technology.

Zhang, Y., Hudson, D., Winden, B., Turnock, S., 2021. Evaluating the Effects of Drift Angle on the Self-Propelled Ship using Blade Element Momentum Theory. Curran Associates, Inc.

Zhang, Y., Winden, B., Hudson, D., Turnock, S., 2022. Hydrodynamic Performance of a Self-Propelled KCS at Angle of Drift Including Rudder Forces. NUTTS Committee.

Zhang, Y., Windén, B., Ojeda, H.R.D., Hudson, D., Turnock, S., 2024. Influence of drift angle on the propulsive efficiency of a fully appended container ship (KCS) using computational fluid dynamics. Ocean Eng. 292, 116537.

Zhang, W., Zou, Z., 2016. Time domain simulations of the wave-induced motions of ships in maneuvering condition. J. Mar. Sci. Technol. 21, 154–166.

Zhu, Z., Kim, B.S., Wang, S., Kim, Y., 2022. Study on numerical PMM test and its application to KCS hull. Appl. Ocean Res. 127, 103327.